

Mechanical compaction mechanisms in the input sediments of the Sumatra Subduction Complex- insights from microstructural analysis of cores from IODP Expedition- 362

Sivaji Lahiri^{1*}, Kitty L. Milliken², Peter Vrolijk³, Guillaume Desbois¹, Janos L. Urai¹

¹Institute of Tectonics and Geodynamics, RWTH Aachen University, Germany, Lochnerstrasse 4–20, 52056, Aachen, Germany

²Bureau of Economic Geology, The University of Texas at Austin, Austin, TX, 10611, USA

³Applied Ocean Science and Engineering, Woods Hole Oceanographic Institution, Woods Hole, MA, United States

* Corresponding author: sivaji.lahiri2@gmail.com

Abstract

The input sediments of the North Sumatra subduction zone margin, drilled during IODP Expedition 362, exhibit remarkable uniformity in composition and grain size over the entire thickness of the rapidly deposited Nicobar Fan succession (sea-floor to 1500 mbsf), providing a unique opportunity to study the micromechanisms of compaction. Samples were prepared from dried core samples from sites (U1480 and U1481) by both Ar-ion cross-section polishing and broad-ion beam cutting, and imaged with a field-emission Scanning Electron Microscope (SEM). Shallowest samples (sea-floor to 28mbsf) display a sharp reduction in porosity from 80% to 52% due to collapse of large clay-domain/matrix pores associated with rotation and realignment of clay-platelets parallel to the bedding plane. The deeper succession (28mbsf to 1500mbsf) exhibits less rapid reduction in porosity from 52% to 30% by the progressive collapse of silt-adjacent larger pores by bending and subsequent sliding/fracturing of clay particles. In addition, there is a correlated loss of porosity in the pores too small to be resolved by SEM.

Clastic particles show no evidence of deformation or fracturing with increasing compaction. In the phyllosilicates, there is no evidence for pressure solution or recrystallization: thus, compaction proceeds by micromechanical processes. Increase in effective stress up to 18 MPa (~1500mbsf) causes the development of a weakly aligned phyllosilicate fabric mainly defined by illite clay particles and mica grains, while the roundness of interparticle pores decreases as the pores become more elongated. We propose that bending of the phyllosilicates by intra-particle slip may be the rate-controlling mechanism.

Pore size distributions show that all pores within the compactional force chain deform, irrespective of size, with increasing compactional strain. This arises because the force chain driving pore collapse is localized primarily

31 within the volumetrically dominant and weaker clay-rich domains; pores associated with packing around isolated
32 silt particles enter into the force chain asynchronously and do not contribute preferentially to pore loss over the
33 depth range studied.

34 Introduction

35 Muds are fine-grained sediments (>50% of particles <63µm diameter) comprising platy detrital clay minerals and
36 equidimensional detrital grains such as quartz, feldspar, calcite, etc. (Nakano, 1967; Hesse, R., 1975; Sintubin,
37 1994). Understanding the mechanical, chemical, and microstructural properties of mud and mudstone is of great
38 interest for rock property prediction in basic earth science, in exploration, subsurface integrity studies and
39 geotechnical engineering (Yagiz, S., 2001; Aplin and Macquaker, 2011; Lazar et al., 2015). The chemical and
40 physical behavior of marine muds plays a critical role in defining the geometry of accretionary prisms, locating
41 the décollement for fault rupture (Vrolijk, 1990; Chester et al., 2013) and understanding subduction zone
42 earthquakes and tsunamis (Dean et al., 2010; Chester et al., 2013; Hüpers et al., 2017).

43 Marine mud is deposited with a highly porous isotropic fabric (Bowles, 1969; Bennett et al. 1981; 1991);
44 depositional porosity in mud is about twice as high as in sand (e.g., Velde, 1996, Lundegard, 1992). In contrast,
45 mudstones have low porosities, modal pore sizes measured in nm, and an absence of textural controls on porosity
46 (e.g. Aplin et al., 2006; Milliken et al., 2012; 2013). The processes in this dramatic evolution of porosity have
47 similarities to compaction of sand to sandstone, comprising a combination of compaction and cementation
48 (Milliken and Day-Stirrat, 2013), although the much smaller, elongated phyllosilicate grains increase the role of
49 clay-bound water in the process (Karaborni et al., 1996). Whereas a refined and somewhat predictive
50 understanding exists for porosity evolution in sand and sandstones (e.g., Lander and Walderhaug, 1999; Paxton et
51 al., 2002; Lander et al., 2008; Ajdukiewicz and Lander, 2010, Desbois et al., 2011), such a model is at best
52 preliminary for muds and mudstones (Pommer and Milliken, 2015; Milliken and Olson, 2017). It seems clear that
53 the composition of the grain assemblage importantly sets the stage for porosity evolution in muds (Milliken, 2014),
54 cementation being the greatest in muds with abundant biogenic debris. In contrast to sandstones, however,
55 cementation is far less common globally in mudstones (Milliken, 2019), leading to the notion that mechanical
56 compaction may be far more important in muds. In addition, depositional environment also strongly controls
57 porosity evolution, compaction and diagenesis in mudrocks (e.g. Burland, 1990; Baruch et al., 2015; Delle Piane
58 et al., 2015) as the initial clay and rigid grain compositions significantly affect both compaction (as this manuscript
59 shows) and subsequent diagenetic alteration due to variations in composition. Establishing the expected
60 compaction behavior for muds in a setting of well-constrained mud properties is an essential contribution that our
61 study hopes to serve.

62 Investigations of mud and mudstone compaction are usually based on proxy data, such as velocity or density,
63 rather than direct measurements of porosity (e.g., references in Mondol et al., 2007). Direct measurement of
64 porosity can be broadly classified into two categories: 1) laboratory experiments; (e.g., Mitchell, 1956; Bennett et
65 al. 1981; Griffiths and Joshi, 1989; 1990; Vasseur et al. 1995; Mondol et al. 2007; Fawad et al. 2010; Emmanuel
66 and Day-Stirrat, 2012), and 2) studies on natural samples (e.g., Meade, 1964; Ho et al., 1999; Aplin et al. 2003;
67 2006; Day-Stirrat et al., 2008; 2010; 2012; Milliken et al, 2012; 2013). A common shortcoming of studies on

68 natural samples is the assumption that the bulk porosity is a direct measure of compaction although porosity loss
69 has contributions of both compaction and cementation (Ehrenberg, 1989; Lundegard, 1992; Paxton et al., 2002),
70 and this can only be accomplished by petrographic inspection (Milliken and Curtis, 2016). Experimental studies
71 generally avoid this shortcoming by the use of lab-produced particle packs that undergo no chemical change during
72 the experiment. Studies of shallowly buried units (like the present study) are the ones most likely to avoid the
73 complication of cementation, especially if temperatures are low and bulk grain assemblages are siliciclastic
74 (Milliken, 2008, 2014).

75 Previous studies report contrasting ideas about the mechanisms of mechanical compaction of mud. Some studies
76 conclude that rotation is the dominant particle scale mechanism for mechanical compaction (Bowles et al., 1969;
77 Oertel and Curtis, 1972; Vasseur et al., 1995), although other particle scale-deformation mechanisms were not
78 investigated by these authors. A few studies state that burial compaction significantly increases the alignment of
79 phyllosilicate (clay and mica) parallel to the bedding planes (Bowles et al., 1969; Oertel and Curtis, 1972; Vasseur
80 et al., 1995) (a detailed review of the previous studies on mechanical compaction is given in Supplementary data-
81 1). Other studies contrastingly narrate that, intense mechanical compaction (i.e. effective stress) has a limited
82 impact on the development of phyllosilicate fabric in mud (Ho et al., 1999; Aplin et al., 2006; Day-Stirrat et al.,
83 2008; 2011). In addition, earlier authors conclude that an increase in effective stress causes preferential loss of
84 larger pores, and as a result, the mean porosity of the samples decreases (Delage and Lefebvre, 1884; Griffiths and
85 Joshi, 1989; 1990; Emmanuel and Day-Stirrat, 2012). With increasing consolidation stress, bimodal pore size
86 distribution curve shifts toward smaller pore sizes as larger pores rapidly collapse (Griffiths and Joshi, 1989; 1990;
87 1991). These studies investigated the changes in particle alignment and reduction in porosity (Ho et al., 1999;
88 Aplin et al., 2006; Day-Stirrat et al., 2008; 2011) but without imaging the evolution of pore morphology with
89 increasing compactional strain. Moreover, in previous studies, the authors mainly performed laboratory
90 consolidation experiments on lab produced particle packs, and used conventional techniques, such as mercury
91 intrusion porosimetry, high-resolution X-Ray pole figure goniometry (HRXTG) to understand the evolution of
92 pore size distribution with consolidation stress (Ho et al., 1999; Aplin et al., 2006). Studies on naturally compacted
93 samples are rare. This is where this study aims contribute.

94 We received 55 mud samples from drill cores collected during IODP Expedition 362 west of the North Sumatra
95 subduction zone margin and investigated the evolution of petrographic microstructure and pore morphology as a
96 function of compactional strain. Apart from general implications for global mudrocks, we hope this investigation
97 will also contribute to studies that seek to predict rock properties in the deeper subsurface at the Sumatra
98 subduction front.

99

100 Geological background and drilling

101 The Sumatra subduction zone extends 5000km from the Andaman-Nicobar Islands in the northwest to the Java-
102 Banda arc in the Southeast (Fig. 1a and b) (Prawirodirdjo et al., 1997; Hippchen and Hyndman, 2008). The trench

103 of the Sumatra subduction zone (Fig. 1a) developed on the subducting Indo-Australian Plate at a convergence rate
104 of 5.5 cm/yr in the north and 7.23 cm/yr in the South (Ghosal et al., 2014; Moeremans, and Singh, 2015).

105 On 26th December 2004, the west coast of Northern Sumatra recorded one of the largest earthquakes (Mw-9.3) in
106 the 21st century, generating a devastating Tsunami in the Indian Ocean (Ammon et al., 2005; Lay et al., 2005).
107 Understanding the mechanism(s) behind this unprecedented event was the central idea behind IODP Expedition
108 362 (Fig. 1). The main objective of the expedition was to collect core and log data of the incoming sedimentary
109 succession of the Indo-Australian oceanic plate to understand the seismogenic process related to the margin (Dugan
110 et al., 2017; McNeill et al., 2017). During the expedition in 2016, drilling was performed on two sites U1480
111 (Holes E, F, G and H) and U1481 (Hole A) located on the oceanic plate west of the North Sumatra subduction
112 margin and east of the Ninety East Ridge (Fig. 1a, b) (Dugan et al., 2017). The drilling sites recovered a complete,
113 1.5 km thick sedimentary section from late Cretaceous to Pleistocene down to the basement of basaltic crust
114 (Dugan et al., 2017; McNeill et al., 2017).

115 The input sedimentary section of the Sumatra subduction zone comprises the distal part of the trench wedge,
116 Nicobar fan sequence, and pre-fan pelagic section on the basaltic crust at the bottom (Dugan et al., 2017; McNeill
117 et al., 2017). At Site U1480, the entire recovered section was categorized into six lithological entities, Units I to
118 VI (Fig. 1c) (McNeill et al., 2017). Unit I (0 to 26.72 mbsf) consists of unconsolidated calcareous clay, silty clay
119 with alternating fine sand (McNeill et al., 2017). Unit II from 26.72 to 1250 mbsf consists of three subunits (IIA,
120 IIB and IIC) and mainly exhibits alternating fine-grained sand and silty clay to silt (McNeill et al., 2017). Unit III
121 (1250 ~ 1327 mbsf) is divided into two subunits: Unit IIIA and IIIB (McNeill et al., 2017). Unit IIIA consist of
122 thin to medium-bedded, gray-green or brown mudstone and intercalated siltstone, and Unit IIIB is composed of
123 reddish-brown tuffaceous silty claystone with fragmented sponge spicules and radiolaria (McNeill et al., 2017).
124 The boundary between Units IIIA and IIIB (1310 mbsf) at this site marks the base of the Nicobar Fan and the
125 beginning of the thin pre-fan succession (Pickering et al., 2020). Units IV, V, and VI include volcanoclastic rocks
126 with tuffaceous sandstone, conglomerates, and basaltic oceanic crust, respectively. At Site U1481, the pre-fan
127 succession was not encountered and a Unit III, a thicker equivalent of Subunit IIIA at Site U1480, represents the
128 material of the lower Nicobar Fan (see Figure F15, in Site U1481 report; McNeil et al., 2017). Units IV, V and VI
129 at U1481 comprise tuffaceous volcanoclastic sand, calcareous ooze and basaltic oceanic crust. This study is
130 restricted to the Nicobar fan sequence that comprises Unit I, II, and IIIA (equivalent to Unit-III at U1481).

131 X-ray diffraction (XRD) and bulk rock analysis at Site U1480 (in Units I and II) show a clay mineral assemblage
132 dominated by illite, with little smectite and chlorite (Table-2; Supplementary data-2) (Rosenberger et al., 2020).
133 The smectite content decreases with depth with the mean value of 33 wt% in Unit I and 17 wt% in Unit II (Table
134 1, Fig. 2a) (Rosenberger et al., 2020). However, the relative abundance of smectite content increases sharply in
135 Unit IIIA with a mean value of 73 wt% (Fig. 2a). The illite percentage in the clay assemblage at U1480 drilling
136 site increases down section from Unit I to Unit II with a mean of 49 wt% to 59 wt%; whereas it decreases in Unit
137 IIIA with a mean of 19 wt% (Fig. 2b). The expandability of the illite/smectite (I/S) mixed-layer clay in Unit-I at
138 U1480 ranges 48% to 68.8% with a mean value of 62%. However, the mean expandability of the I/S mixed layer
139 clay increases down section up to a mean value of 88% in Unit-IIIA (Supplementary data-3). An increase in I/S
140 expandability with increasing depth signifies an opposite trend to the one expected for burial diagenesis

141 (Rosenberger et al., 2020). Clay mineralogy in the lower fan muds of Unit III at Site U1481A contains an average
142 of 37% smectite and 37% illite (Rosenberger et al., 2020) (Fig.2a, b, c and d). At the site U1481A, the mean
143 expandability of I/S mixed layer clay is obtained 64% in Unit-II and 73% in Unit-III. The increase in I/S
144 expandability with depth is likely related to an increase in amount of smectite content due to alteration of volcanic
145 ash.

146 The Nicobar fan sequence exhibits almost compositionally homogeneous (silt/clay ratio; mostly ‘silty-clay’)
147 subunits with uniform grain size (McNeill et al., 2017), and also a history of rapid deposition (125-290 m/my;
148 Backman et al., 2019). The sedimentary sequence does not exhibit any evidence of upliftment, and currently occurs
149 at maximum burial depth. The drilling sites are 255 km away from the deformation front, thus the samples are
150 undisturbed by tectonic faulting (Fig.1b). In addition, owing the scarcity of biogenic grains and the low
151 temperatures encountered (<68°C), cementation is only observed as highly localized concretions (Red coloured
152 symbols in Fig.2e, f, g, and h) (McNeil et al., 2017; Torres et al., 2022). Such a homogeneous sedimentary
153 succession extending across 1.5 km depth is rare in sedimentary basins. Hence, these samples provide us with a
154 unique opportunity to study depth-wise variation in microstructure as a function of vertical effective stress with
155 few complications from multiple causes of porosity loss.

156 Sampling and Methods

157 This study is based on two sample sets that were obtained from Sites 1480 (Holes E, F, G, and H) and 1481 (Hole
158 A) independently, and analyzed by slightly different methods. The first sample set (33 mud samples; depth 1.24
159 to 1300 mbsf) was prepared using Broad Ion Beam polishing and analyzed using Scanning Electron Microscope
160 (BIB-SEM technique) at RWTH Aachen University, Germany. The second sample set (22 samples; depths 6.25
161 to 1493.30 mbsf) was prepared using Ar-ion cross-section polishing and imaged by field-emission SEM at the
162 Bureau of Economic Geology (BEG) at the University of Texas at Austin. In Fig.2e, and f, blue points are
163 representing Shipboard MAD (Moisture and density) porosity vs depth data for mudstone samples recovered from
164 Sites U1480 and U1481, and yellow points are describing analysed samples at Aachen and BEG. Respective core
165 description of these 55 mud samples and their bulk mineralogy data are tabulated in Supplementary data-4.

166 BIB-SEM technique (analysis of the first set of samples, Aachen University)

167 Sample preparation for BIB-SEM and imaging

168 After drilling, the samples were stored at Kochi drill core repository (IODP), Japan for four years (2016 ~ 2020)
169 at the refrigerated storage areas maintaining the temperature of ca. 4°C and 80% humidity (http://www.kochi-core.jp/en/iodp-curation/curation-sop_2.html). We received a total of 33 freeze-dried mud samples (SN-1 to SN-
170 33 in Table-1) for analysis at Aachen. The samples were collected using a tube inserted perpendicular to the cut
171 face of the drill core in such a way that the notch of the tube identified the top of the sample so the orientation of
172 bedding planes for each sample was known. In Fig. 1d, a tube sample received from the IODP repository is shown,
173 where the red line on the top of the tube identifies the notch. Subsamples (10 x 5 x 2 mm³) were cut from the
174 individual freeze-dried samples using a razor blade. These subsamples were pre-polished using silicon carbide
175 (SiC) paper to reduce the roughness of the surface down to 10 µm. Further, Broad Ion Beam (BIB) polishing was
176

177 carried out using a JEOL SM-09010 cross-section polisher for 10 hours at 6 kV and 150 μ A. BIB reduces surface
178 damage by removing a 100 μ m thick layer to generate a high-quality polished cross-section of 1-2 mm² with a
179 topography less than 5 nm (Desbois et al., 2009).

180 After polishing, the BIB cross-sections were coated with tungsten and imaged with a Zeiss Supra 55 SEM with
181 SE2, BSE, and EDX detector (Supplementary data-5). SE2 images were used to image porosity, while for
182 identifying phases BSE images are combined with an EDX map as well as EDX point analysis. For each cross-
183 section, we made mosaics of hundreds of SE2 and BSE images at a magnification of 20,000x (~14.3 nm pixel
184 value) and 10,000x respectively, with an overlap of 20% to 30%, (Klaver et al., 2012; 2015; 2016; Hemes et al.,
185 2013; 2015; 2016; Laurich et al., 2014). The mosaics are stitched together using Aztec software preserving the
186 original pixel resolution. Finally, these stitched images are used for the segmentation of pore spaces, minerals, and
187 other respective analyses.

188 Image segmentation and pore analysis

189 For quantifying porosity and pore morphology, individual SE2 image mosaics were segmented using a ‘seed and
190 grow’ algorithm (Adams and Bischof, 1994) implemented with a MatLab code (Jiang et al., 2015; Schmatz et al.,
191 2017) (Supplementary data-5). The ‘seed and grow’ algorithm works based on the difference in intensity of
192 greyscale value in an image (bright = minerals, dark = pores). After automatic segmentation, individual pores in
193 SE2 images are manually corrected if required.

194 Similarly, using ImageJ software (threshold toolbox and machine learning algorithm), segmentation of the
195 individual mineral phases was carried out combining BSE images and EDX elemental maps. While quartz, calcite,
196 pyrite, mica minerals are efficiently segmented using these tools, feldspars are found difficult to segment because
197 of similar composition as clay (Supplementary data-6, 7 and 8). Finally, corrected pore segmented SE2 mosaics
198 are overlaid on the phase maps using the ‘georeference’ tool of QGIS (<http://qgis.osgeo.org>), (Supplementary data-
199 6, 7 and 8).

200 Pore detection resolution (PPR) and representative area analysis (REA)

201 ‘Practical pore detection resolution’ (PPR) indicates the pore sizes above which one can assume to detect 100% of
202 the pores present in the SE2 mosaic (Klaver et al., 2012). In agreement with earlier results using this instrument
203 (Klaver et al., 2012; 2015; 2016; Hemes et al., 2013; 2015; 2016; Laurich et al., 2014), we found PPR of ~2000
204 nm² and ~8500 nm² for the magnification of 20,000x and 10,000x images, respectively, corresponding to 10pixel.

205 After segmenting all minerals, representative elementary area analysis (REA) was performed using the box
206 counting technique on mineralogical phase maps (Kameda et al., 2006; Klaver et al., 2012). Similar steps are also
207 followed for determining a representative elementary area for SE2 images. The estimated REA values using SE2
208 and BSE mosaics for the analysed 33 mudstone samples are documented in Supplementary data-9.

209 It should be noted that, we estimated porosity, pore morphology, pore size, and statistical distribution of pores
210 using image analysis technique on 2D images collected using BIB-SEM technique. In reality, pores are non-

211 spherical 3D objects, which are cut through at a random point perpendicular to the bedding plane to acquire 2D
212 image dataset. Hence, it may add biases to the obtain results. We plotted ship-board measured MAD (moisture and
213 density) porosity vs depth (Fig.2e) and also BIB-SEM porosity vs depth for the analysed samples (Fig.3a), where
214 MAD porosity documents bulk porosity for the sample, and BIB-SEM porosity represents 2D counterpart of the
215 non-spherical 3D pores/porosity. It is observed, both plots are following similar trend. Therefore, we may assume
216 that porosity and pore size distribution obtained from 2D image analysis could be a representative of the bulk rock
217 porosity and 3D pore size distribution of the samples. In addition, the estimated REA can also be assumed
218 reasonably good to document bulk pore characteristics of the sample.

219

220 Ion polishing and SEM technique (second set of samples; BEG, UT Austin).

221 22 Samples (SN-34 to SN-55 in Supplementary data-4) were taken shipboard from the sample half of the still-wet
222 core in small plastic tubes (similar to the ones used for the sample set at Aachen) inserted into the core by manual
223 pressure. The tubes were removed from the core and sealed in plastic bags. In the laboratory at the BEG, sample
224 bags were opened and the muds were allowed to dry slowly in the tubes over several weeks. No discernible
225 shrinkage was observed as the dried core pieces still fully filled the tubes. The tubes were carefully removed and
226 a small cube (approximately 0.5 to 1 cm³) was cut using a sharp knife and small hand saws; an orientation mark
227 was placed on the cube to indicate the bedding direction. Bed-perpendicular surfaces were prepared by Ar-ion
228 cross-section polishing, using the Leica EM TIC020 triple ion beam miller and coated with Ir for imaging. Manual
229 placement of the cut cubes into the ion mill is not precise so the ion-polished surfaces have slight variation from
230 perpendicular to bedding. Pore imaging was performed on the FEI Nova NanoSEM 430 using the in-lens SE
231 detector, a 30 µm aperture, 15 KeV accelerating current, a working distance of around 5–6 mm, and an
232 intermediate-range sample current (spot size = 3, mid-range for the instrument). Randomly selected views
233 (typically 3-6) of all samples were collected at 6kx machine magnification; additional views illustrating pore types
234 and pore/grain relationships were made at 10kx to 30kx (machine magnification).

235

236 Results

237 Estimating compaction strain from MAD-porosity data

238 During expedition, mass and volume of the mud samples were estimated for both wet and dry state using high
239 precision electronic mass balance, and helium pycnometer (http://www-odp.tamu.edu/publications/tnotes/tn37/tn37_8.htm), respectively. Further, using the obtained mass and volume dataset for wet and dry conditions, bulk
240 MAD (moisture and density) porosities were estimated. However, for the present study, we directly obtained ship-
241 board MAD porosity data for the analysed samples from IODP website.
242

243 Shipboard MAD porosity versus depth data for mud samples exhibits a sharp reduction in porosity from 80% to
244 52% from the seafloor to 28 mbsf (Fig.2e). Deeper samples display a comparatively smaller reduction in porosity
245 of approximately from 52% to 30% over a depth range of 28 to 1500 mbsf (Fig.2e and f).

246 We calculated compaction strain using the shipboard MAD porosity data following a method proposed by Nollet
247 et al., 2005, and subsequently used by Neagu et al., 2010 (Fig.2g and h), assuming 1D consolidation and no change
248 in solid volume. The compaction strain (ϵ_c) is then computed as:

$$249 \quad \epsilon_c = \frac{1-\phi_0}{1-\phi_1} \quad (\text{Eqn-1})$$

250 Here ϕ_0 = initial porosity, and ϕ_1 = final porosity. Our samples from sites U1480 and U1481 show no evidence of
251 tectonic faults (McNeill et al., 2017), supporting our assumptions. We considered the initial porosity ϕ_0 as the
252 MAD porosity at 0.6 mbsf depth ($\phi_0 = 80\%$). Compaction strain following Eqn-1 (Table 2; Supplementary data-
253 9), is plotted against depth in Fig.2g and h. Compaction strain increases from 1 to 2.05 from the seafloor to 28
254 mbsf (i.e. Unit I), and from 2.00 to 3.05 from 28mbsf to 1500 mbsf (Fig. 2g and h).

255 Another common measure of compaction is the intergranular volume (IGV; Paxton et al., 2002), which
256 corresponds to the sum of intergranular porosity and intergranular cement. In some mudstones, it may be necessary
257 to calculate IGV differently because of the presence of abundant primary intragranular pores and pore-filling
258 bitumen (Milliken and Olson, 2017). In our sample set, cement is absent, and IGV is taken to equal the bulk
259 porosity from shipboard MAD measurements.

260 Compactional porosity loss (COPL), referenced against the original sediment volume, is calculated from the initial
261 primary intergranular porosity (P_i ; 80% in this case) and the IGV as follows (Ehrenberg, 1989, Lundegard, 1992):

$$262 \quad \text{COPL} = P_i - ((100 - P_i) \times \text{IGV}) / (100 - \text{IGV}) \quad (\text{Eqn-2})$$

263 At an IGV of 50%, COPL is 60%; in the deepest samples in the Nicobar fan (IGV of around 30%) COPL is 70%
264 (Table 2, Supplementary data-9).

265 Description of grain microstructure and pore morphology

266 To have consistency in the data set, we prepared SE2 mosaics for all samples from the Aachen sample set at
267 20,000x magnification covering an average $100 \times 100 \mu\text{m}^2$ area (Table 2). In addition, to examine the effect of
268 magnification on BIB-SEM porosity and representative area analysis (REA), three samples (i.e. SN-7, SN-15, and
269 SN-29) were also imaged each at 5,000x and 10,000x magnification (Table 2), respectively. A decrease in
270 magnification and resolution reduces visible BIB-SEM porosity.

271 We observed consistent results for the REA analysis. For SE2 mosaics, REA varies between $45 \times 45 \mu\text{m}^2$ to 85×85
272 μm^2 at 20,000x magnification, and for segmented phase maps, REA varies between $90 \times 90 \mu\text{m}^2$ to $130 \times 130 \mu\text{m}^2$

273 at 10,000x magnification (Table 2). In the UT sample set, the standard images taken at 6kx with machine
274 magnification are $49.7 \times 45.7 \mu\text{m}^2$ in size, so these images are also within the estimated REA range.

275 Based on EDX elemental map or point analysis, it is observed that six mineral phases occur in significant amounts
276 in the Sumatra samples, as detrital particles: Quartz, feldspar (K-feldspar, Na-feldspar), calcite, pyrite, micas
277 (muscovite, biotite, and chlorite), and clay. Based on ship-board XRD analysis data, it is known that clay size
278 particles are dominantly illite in composition. The average clay percentage in these mudstone samples varies
279 between 65% to 75%. Samples SN-1 (77%) and SN-4 (76%) are slightly enriched in clay content, whereas SN-7,
280 SN-9, SN-17, SN-28, SN-29, and SN-31 contain less clay (<65%) (Table 2; Supplementary data-9).

281 Using BIB-SEM and automatic pore segmentation techniques, an average of >30,000 pores has been detected for
282 each individual sample in the Aachen sample set at 20,000x magnification. Correlating with the MAD data set,
283 the estimated BIB-SEM porosity reduces from 32% to 19% over a depth range of seafloor to 28 mbsf, while the
284 deeper samples display a smaller reduction from 19% to 10% over a depth range of 28 to 1500 mbsf respectively
285 (Fig.3a). Consistent with numerous previous studies, the results document a mismatch between bulk measured
286 porosity (MAD) and imaging porosity (BIB-SEM) (e.g., Hemes et al., 2013; Houben et al., 2014; Nole et al., 2016;
287 Oelker et al., 2019) (Supplementary data-9). We plotted BIB-SEM porosity vs MAD porosity and found an
288 approximately linear correlation with coefficient of determination ($R^2=0.8621$) (Fig. 3b).

289 Type of pores

290 Intergranular pores contribute >99% of the total visible porosity. Intragranular pores (see below) are rare. The size
291 and shape of inter-granular pores change during compaction (Supplementary data-10).

292 Intergranular pores are classified (Fig.4) based on grain size (irrespective of mineralogy): 1) Clay domain (matrix)
293 pores, and 2) silt-adjacent pores. Based on the variation in size, clay domain pores are divided further into: 1)
294 Large clay domain pores, pore size $>5 \times 10^5 \text{ nm}^2$, and the pore boundary is defined by more than three clay particles;
295 and 2) small clay domain pores, the pore size $<5 \times 10^5 \text{ nm}^2$ and generally occur in between two/three clay particles
296 (see further details below). Large and small clay domain pores are classified by geometry as: 1) Elongate pores
297 (aspect ratio $>3:1$) and, 2) equant-shaped pores (aspect ratio $<3:1$). Elongate pores consist of: 1) Linear-elongated
298 pores, and 2) crescent-shaped elongated pores. Examples of different clay-domain pore types are shown in Fig. 5,
299 6, and 7.

300 Silt-adjacent pores are categorized in two types: 1) large silt-adjacent pores are $>5 \times 10^5 \text{ nm}^2$ in size, and pore
301 boundaries are defined by more than three particles; and 2) small silt-adjacent pores include pore sizes $<5 \times 10^5$
302 nm^2 , and pore boundaries are defined by two/three particles (see further detail on the modal sizes of these pore
303 types below). Large and small silt-adjacent pores are either: 1) Equant shaped (aspect ratio $<3:1$) or 2) elongated
304 (aspect ratio $>3:1$). Further, elongated silt-adjacent pores consist of: 1) linear-shaped elongated pores and 2)
305 crescent-shaped elongated pores. These pore types are highlighted in Fig. 5, 6, and 7.

306 Change in inter-particle pore morphology with depth

307 *Seafloor to 28mbsf (Unit I)*

308 The shallow mud samples in Unit I are unconsolidated (less compacted) and highly porous (Fig. 5a). Sample SN-
309 1 (1.24 mbsf) has a maximum MAD porosity of 80%. We observe three types of clay particle contacts in the
310 microstructure of SN-1; edge to edge (EE), edge to face (EF), and face to face (FF) contacts (Supplementary data-
311 11). Among them, EF and FF contacts are abundant and EE contacts are rare. The sample exhibits abundant large
312 clay domain pores and large silt-adjacent pores that are equant with smooth edges and a rounded pore perimeter.
313 The sample also contains abundant linear-elongated and equant-shaped small clay-domain pores. Crescent-shaped
314 small clay domain pores are rare in the microstructure of this sample. Equant-shaped, small silt-adjacent pores are
315 abundant. In addition, linear elongated and crescent-shaped small, silt-adjacent pores are also commonly observed
316 (Fig.5a; Supplementary data-10).

317 With increasing compaction strain ($\epsilon_c = 1.119$) and depth (5.1 mbsf; Supplementary data 9), porosity (MAD)
318 reduces to 75% and corresponding COPL=19% (sample SN-2; Fig. 5b, Supplementary data-12). The
319 microstructures of SN-2 displays almost similar characteristics as observed in the earlier sample SN-1, although
320 there are fewer large clay domain pores in SN-2 than SN-1. Linear elongated and equant-shaped small clay domain
321 pores are common (Supplementary data-10), but crescent-shaped small clay domain pores are rare. The
322 microstructures of SN-2 exhibits abundant equant-shaped large and small silt-adjacent pores.

323 With an increase in compaction strain to $\epsilon_c \sim 2.00$ (28 mbsf), the sample microstructure is dominated by FF contacts
324 (Fig. 5c), and EE and EF contacts are rare (Supplementary data-11). Additionally, large clay-domain pores become
325 sparse or infrequent in the microstructure (Fig. 8). Crescent-shaped, small clay domain pores in the microstructure
326 are rare, whereas equant-shaped small clay domain pores are common. Both small and large silt-adjacent pores
327 exhibit equant shapes (Fig. 8d, e and f). The sample analysed at the base of Unit I (SN-6; 28 mbsf) contains rare
328 large clay-domain pores and abundant FF contacts (Fig. 5c; MAD porosity = 54% and COPL = 55%).

329 *28 mbsf to 1500 mbsf (Units II and III)*

330 Mud samples from the deeper part of the Nicobar fan section are more compacted than shallower samples. We
331 analyzed a total of 29 samples using BIB-SEM at Aachen and 18 samples using the field emission SEM at UT
332 Austin from this section. An increase in compactional strain from 2.00 to 3.15 over a depth range of 28 to 1500
333 mbsf causes a porosity reduction (MAD) of 54% to 28%, and the corresponding change in average COPL is 55%
334 to 72%. The microstructure of these samples is dominated by FF contacts among clay particles; EF and EE contacts
335 are rare (Supplementary data 11; Fig. 6 and 7 b, c). All samples exhibit abundant small linear-elongated clay
336 domain pores between two parallel clay sheets (Fig. 8b). Equant-shaped small, clay domain pores are rarely
337 observed below 150 mbsf depth ($\epsilon_c > 2.4$). Crescent-shaped, small, clay domain pores are rare at shallow depth but
338 become abundant with an increase in compactional strain $\epsilon_c > 2.95$ (871.87 mbsf) as the surrounding clay particles
339 are bent (Fig.6). In addition, large clay domain pores in these samples are rarely observed in the vicinity of silt
340 clasts (Fig.6, Supplementary data-13).

341 Below 100 mbsf ($\epsilon_c = 2.20$), silt-adjacent small pores are dominantly equant shaped, but below 300 mbsf ($\epsilon_c > 2.5$)
342 silt-adjacent small pores are dominantly linear-elongated (Fig. 8e). Crescent-shaped, small, silt-adjacent pores are
343 common in all samples. Large silt-adjacent pores are dominantly equant above 200 mbsf depth ($\epsilon_c < 2.40$) and
344 commonly linear-elongate below 400 mbsf depth ($\epsilon_c > 2.5$) (Fig.8f). It appears that, due to an increase in
345 compactional strain, the shape of the silt-adjacent pores changes from equant to linear-elongated (Supplementary
346 data-10). In samples with more silt, equant-shaped small and large, silt-adjacent pores can persist at greater depths
347 (Fig. 8e and f).

348 Below 28 mbsf ($\epsilon_c > 2.0$), the number of large silt-adjacent pores in the microstructures decreases. Comparing
349 samples SN-8 (74.07 mbsf and $\epsilon_c = 2.09$) and SN-32 (1267.14mbsf and $\epsilon_c = 3.15$) illustrates how the number of
350 large, silt-adjacent pores decreases with depth (Fig. 6a, and c) when the clay fraction (Supplementary data 9) is
351 comparable. This relationship is apparent even in samples separated by a smaller depth difference (SN-49 from
352 959.14 mbsf and SN-55 from 1433.36 mbsf; Fig. 7b and c). While the number of large pores diminishes, the
353 maximum size of the large silt-adjacent pores remains constant (10^7 nm^2 ; Supplementary data 14).

354 Variation in the orientation of pores and grains due to compactional strain

355 We examined the change in orientation of the long axis of pores with increasing compaction strain. For all
356 segmented pores, the angle between the long axis and the bedding plane was determined and plotted in rose
357 diagrams (Supplementary data-15). Samples from the seafloor to 28 mbsf exhibit a weak preferred orientation of
358 the long axis of pores with maxima oriented obliquely to the bedding planes. However, below 28 mbsf the samples
359 have a preferred orientation of the long axis of pores aligned subparallel to the bedding plane. Further, due to an
360 increase in vertical effective stress down section below 28 mbsf in Units II and III, the degree of preferred
361 alignment of the long axis of pores only increases to a small amount (Supplementary data-15).

362 We determined the angle between the long axis of individual silt grains and the bedding plane for all samples and
363 plotted the angle in a rose diagram (Supplementary data-15). For quartz, feldspar, and calcite the degree of
364 preferred orientation of the long axis of grains changes little with depth. However, the rose diagrams obtained for
365 mica show weak maxima parallel to the bedding plane and several submaxima oriented obliquely to the bedding
366 plane above 28 mbsf. Preferred alignment of the long axis of mica grains increases at 28 mbsf with a strong
367 maximum oriented parallel to bedding plane. Below 28 mbsf, further increase in the degree of preferred alignment
368 is small.

369 Size distribution of pores

370 Pore size distributions (Fig. 9) of shallow samples (Unit I) are trimodal. Sample SN-1 has peaks between 10^5 to
371 10^6 nm^2 , 10^6 to 10^7 nm^2 , and 10^7 to 10^8 nm^2 , and SN-2 has peaks from 10^4 to 10^5 nm^2 , 10^5 to 10^6 nm^2 , and 10^6 to
372 10^7 nm^2 . These three pore size regimes correspond to the small clay domain and silt-adjacent pores, large clay
373 domain pores, and large silt-adjacent pores. Samples of Units II and III exhibit bimodal pore size distributions
374 (SN-10, SN-26, and SN-33 in Fig. 9). SN-10 has a peak between 10^5 to 10^6 nm^2 , corresponding to small clay
375 domain and silt-adjacent pores, and 10^6 to 10^7 nm^2 , reflecting large silt-adjacent pores. Large clay domain pores

376 are absent from samples below 28mbsf depth (Units II and III) based on the pore size distributions combined with
 377 image analysis. At the shallow depth, contribution to total porosity by larger silt-adjacent pores is greater
 378 compared to the contribution by small clay domain pores (Fig. 9e and g). The contribution of large, silt-adjacent
 379 pores to total porosity diminishes with depth. Hence, at greater depth, contribution to total porosity by larger silt
 380 adjacent pore is less compared to small clay domain pores (Fig. 9i).

381 Pore size distributions follow a power-law shown on a double logarithmic graph following the equations (Klaver
 382 et al., 2012; 2015; 2016; Hemes et al., 2013; 2015; 2016; Laurich et al., 2014):

$$383 \frac{N_i}{b_i S_{mosaic}} = C S_{pore}^D \quad (\text{Eqn-3})$$

$$384 \log\left(\frac{N_i}{b_i S_{mosaic}}\right) = -D \cdot \log(S_{pore}) + \text{Log } C \quad (\text{Eqn-4})$$

385 Where N_i = number of pores with area S_{pore} , b_i = bin size, S_{mosaic} = surface area of the current mosaic, C =constant,
 386 and D = power-law exponent. The resulting power-law exponent (D) varies between 1.70 to 2.00 (Table-2).

387 Effect of texture on porosity, pore morphology, and orientation of pores

388 We analyzed six samples (SN-7, SN-9, SN-17, SN-28, SN-29 and SN-31) that are enriched in silt content compared
 389 to the rest of the mud samples (Supplementary data-9). Silt content has a positive correlation to the total SEM
 390 porosity. For example, sample SN-29 (1172.88 mbsf) exhibits a BIB-SEM porosity of 14% whereas other samples
 391 from a similar depth with less silt exhibit an average BIB-SEM porosity of 12% (Supplementary data-9) at 20000x
 392 magnification. The samples with greater silt content are also enriched in equant-shaped silt-adjacent larger pores
 393 (Fig.10a). We also estimated the orientation of the long axis of pores for these three samples and plotted the
 394 obtained results as rose diagrams (Fig.10b). The obtained results exhibit a relatively weak preferred alignment of
 395 the long axis of pores with respect to the bedding planes (Fig.10b).

396

397 Discussions

398 Effective stress vs porosity: A comparison with experimental study

399 To understand the consolidation mechanisms of the Sumatra sediment, we estimated vertical effective stress
 400 following the steps proposed by Hüpers et al., 2015. Following Terzaghi and Peck, 1948 vertical effective stress
 401 (σ_v') is expressed as:

$$402 \sigma_v' = \sigma_v - P_f \quad (\text{Eqn-5})$$

403 Here σ_v = total vertical stress caused by the overburden load, and P_f = fluid pressure. To compute vertical effective
 404 stress of a layered sediment, we use Eqn 6:

$$\sigma_v' = \sum(\rho_s - \rho_w) \cdot g \cdot \Delta z \quad (\text{Eqn-6})$$

406 where ρ_s = bulk density of the sediment, ρ_w = density of the pore water, Δz = depth interval, and g = gravitational
407 acceleration. During IODP Expedition 362, drilling was performed 255 km away from the deformation front.
408 Although small offset strike-slip faults are evident at the seafloor and in seismic reflection profiles (McNeill et al.,
409 2017), the amount of strain attributed to these fault offsets supports the idea that the maximum horizontal stress is
410 comparable to the vertical stress; there is no evidence in seismic reflection data or from core microstructures for
411 thrust or reverse faults associated with a vertical least principal stress. On this basis, we assume that vertical stress
412 is the maximum principal stress, and that pore pressure is hydrostatic. Bulk density of the sediment ρ_s was acquired
413 from MAD data set obtained from IODP website, and ρ_w was considered as the density of sea-water i.e. 1025
414 kg/m³ (Hüpers et al., 2015).

415 We plotted vertical effective stress vs MAD porosity of 55 mud samples (Fig.11). Fawad et al. (2010)
416 experimentally studied the consolidation behavior of mud with varied proportions of silt and clay. While Sumatra
417 samples follow trends similar to those defined by Fawad et al. (2010), the experimental samples are more
418 compacted than natural Sumatra samples for the same silt content.

419 Clay mineralogy has a significant effect on the compaction behavior of mudstone (Mondol et al., 2007). Mondol
420 et al. (2007) performed compaction experiments using pure smectite and pure kaolinite clay particle packs; as they
421 represent two end members compared to other clay minerals (illite and chlorite) in terms of grain size and surface
422 area. Whereas smectite is the most fine-grained clay and has the largest surface area; whereas kaolinite is the
423 coarsest one and has a smaller surface area compared to all other clay mineral types (Meade, 1964; Mesri and
424 Olson, 1971; Rieke and Chilingarian, 1974). Hence, kaolinite is more compressible than smectite, and clay
425 compaction gradually decreases with increasing the proportion of small size clay particles in the sample (Mondol
426 et al, 2007).

427 Fawad et al., (2010) used clay mixtures of 81% kaolinite, 14% mica, and 5% microcline grains, whereas Sumatra
428 mud samples are mainly composed of >50%-60% of illite and 20%-30% smectite, with only <16%
429 undifferentiated chlorite and kaolinite, and <7% quartz particles. Therefore, due to higher illite/smectite content,
430 Sumatra muds appeared to be less compacted compared to the experimental samples used by Fawad et al. (2010).

431 BIB-SEM porosity vs MAD porosity

432 We note that BIB-SEM porosity is lower than the porosity found from the shipboard MAD data, however the two
433 measurements correlate along a line through the origin. (Fig.3b). The reason for this difference is that MAD
434 porosity measures the total amount of moisture in a much larger sample and accounts for pores much below the
435 PPR and also rare large pores not included in the 1 mm² BIB section. Earlier studies also documented and discussed
436 mismatches between MAD and BIB-SEM measurements (Hemes et al., 2013; Houben et al., 2014; Nole et al.,
437 2016; Oelker et al., 2019). We plotted estimated BIB-SEM porosity and MAD porosity data from earlier studies
438 on Boom clay (Hemes et al., 2013; Oelker et al., 2019); Opalinus clay (Houben et al., 2014); and samples from
439 Nankai trough (Nole et al., 2016). The data for Boom clay and Opalinus clay follow similar trend as Sumatra

440 samples, whereas clay samples from Nankai trough shows a different trend. This could be attributed due to the
441 difference in magnification of imaging of Nankai trough samples.

442 In addition, we plotted clay content vs the difference between the two porosities in Fig.12a. We performed
443 regression analysis using the data set for the 33 mud samples analyzed at Aachen (Fig.12b). First, only two
444 variables i.e., BIB-SEM porosity vs MAD porosity (following Eqn-7); second, we considered three variables MAD
445 porosity, BIB-SEM porosity, and clay content (following the Eqn-8).

$$446 \text{ BIB-SEM porosity} = a * \text{MAD porosity} + c \quad (\text{Eqn-7})$$

$$447 \text{ BIB-SEM porosity} = a * \text{MAD porosity} + b * \text{clay content} + c \quad (\text{Eqn-8})$$

448 The coefficient of determinations (R^2) for Eqn-7 and Eqn-8 are 0.8408 and 0.9262 respectively. These results show
449 that the ratio in porosity depends on depth and clay content.

450 For all samples the BIB-SEM pore size distribution follows a power-law over an interval of three orders of
451 magnitude. We may extrapolate this below the practical pore resolution (PPR; Klaver et al., 2012; Kuila and
452 Prasad, 2013; Wang et al., 2019). Extrapolating our data set down to 3nm pore diameter, it is found that BIB-SEM
453 porosity increases only up to 20%~25%. So, there is still an average mismatch of 15% to 20% between the MAD
454 porosity and extrapolated BIB-SEM porosity. The fall off from the normal trend in log-log pore size distribution
455 plots (Fig.9b) for the shallow depth (Unit-I) samples suggest that also large pores are uncounted in the data set.
456 The mud samples from Unit-I contains forams that are rare or absent in the deeper section (Supplementary data-
457 16a, b, c, and d), and part of missing pore volume can be attributed to the intact forams that may be missed due to
458 the small size of the BIB SEM sample.

459 Another important aspect which can incur mismatch in the data set is drying artefacts. In the past, Desbois et al.,
460 2014 performed detailed study on drying artefacts of mudstone samples using Cryogenic BIB-SEM technique.
461 They identified four types of drying damages (Type-I, II, III and IV) that can develop during drying of a mudstone.
462 Type-I and type-II drying damage respectively develops at clay/clay particle interfaces with tip to long axis contact,
463 and at clay/clast interfaces. Heterogeneous deformational behaviour or shrinkage strain of clay and/or non-clay
464 mineral grains can cause building up stress at the boundary during drying to develop these drying artefacts. Type-
465 III drying artefacts are large cracks that develops within the clay matrix itself. Type-IV drying artefacts are the
466 very small damages that modify pore morphology during drying. Among all of them, Type-II and III are the most
467 spectacular and large enough to modify microstructure significantly. The morphology of the type-II and III drying
468 artefacts are characterized by large irregular shaped very elongated pores with serrated pore boundaries. However,
469 in the present study, the large clay domains and silt-adjacent pores in all samples potentially show smooth edges
470 and rounded pore tip-end, which are incompatible with the typical morphologies of the drying artefacts (Fig.5, 6
471 and 7). Hence, drying artefacts appear to be less important in the context of mismatch of MAD porosity and BIB-
472 SEM porosity.

473 Shallow-depth samples from Unit-I are richer in smectite content compared to the deeper samples. Moisture and
474 density method (MAD) generally overestimate the measured porosity of the sediment due to release of interlayer

475 residing H₂O if the sediment contains abundant hydrated minerals such as smectite (Brown and Ransom, 1996;
476 Dutilleul et al., 2020). Hence, small enrichment of smectite content at the shallow depth samples (Unit-I) may
477 have somewhat resulted in overestimation of the MAD porosity in the study.

478 Micromechanical model for porosity reduction

479 Sharp reduction in porosity at the shallow depth from the seafloor to 28 mbsf

480 High porosity (80% MAD; 32% BIB-SEM) in the shallowest sediments is attributed to large pores in the samples
481 created by abundant EE and EF particle contacts (Fig. 5a and 7a). These contacts are unstable and easily collapse
482 under low effective stress to form FF contacts, resulting in a rapid porosity decrease within the first 28m of burial
483 (Supplementary data-11). This deformation is apparent from the reduction of large clay domain pores observed
484 over this interval (Fig. 8; Supplementary data-10). Collapse of pores surrounded by EE and EF contacts is further
485 recognized by the progressive alignment of clay particles into the bedding plane, which promotes the increase in
486 number of elongated, small, clay domain pores parallel to the bedding plane. Each of these observations is
487 consistent with rotation of clay particles into the bedding plane as these large clay-domain pores collapse.

488 Mechanism of porosity reduction from 28 mbsf to 1500 mbsf

489 Below 28 mbsf to >1500 mbsf, porosity continues to decrease from 52-30% (MAD) but at a reduced pace. SEM
490 observations suggest that this porosity decline results from the progressive loss of silt-adjacent pores with large
491 silt-adjacent pores lost before small ones (Fig. 8), although they remain present in common abundance to 1200
492 mbsf. Small clay domain pores are abundant throughout the section, and the large clay domain pores were lost
493 above 28 mbsf.

494 Within the population of silt-adjacent pores, the large, equant pores are most susceptible to collapse (Fig. 8). Large,
495 elongate pores persist in abundance, both in linear and crescent geometries. While it seems plausible that large,
496 equant pores collapse to form large, elongate pores, no corresponding increase in the elongate pore population is
497 observed. Large, elongate pores may collapse further and become small silt-adjacent pores. Microstructural
498 evidence supports the idea that large equant pores collapse as surrounding clay particles within clay-rich domains
499 bend and shrink the size of the remaining pore (Fig.13), and that the collapse results in an increasing aspect ratio
500 of the pore.

501 Frequently, bent clay particles are observed on the top of larger silt-adjacent pores. In the clay microstructure,
502 large silt-adjacent pores act as a zone of heterogeneous strain localization. Hence, the larger silt-adjacent pores are
503 more susceptible to exhibit bent clay than the smaller pores in the clay matrix (Fig.13a to f). With increasing
504 vertical effective stress two situations can arise which are demonstrated in the model shown in Fig.13g
505 respectively. With an increase in effective stress, the bent clay particles can lose frictional resistance from the
506 sidewall (Fig.13a and b) and as a result, the bent clay particles can slide down to fill the larger silt-adjacent pore
507 space (Fig.13g-(iii)). Secondly, with an increase in vertical effective stress bent clay particles may develop
508 fractures (red lines in Fig.13g-(iv)) and can subsequently collapse within the larger silt-adjacent pore space to
509 reduce the porosity of samples (Fig.13g-(v)). For example, Fig.13a represents fractured bent clay on the top of the

510 larger silt adjacent pore (shown by white arrow). Similarly, in Fig.13e, two small clay particles are fallen inside
511 the larger silt adjacent pore space, and on top of them there presents another bent clay particle (shown by white
512 arrow). Fig.13f represents a bent clay particle wrapping on the top of two quartz particles, and inside the space
513 between two quartz particles is filled by four small clay platelets. It appears to be a paleo larger silt-adjacent pore
514 filled by fractured clay platelets. If we carefully look within the pore space between two equant quartz grains in
515 Fig.13f, four small clay particles exist, which may have developed due to the fracturing of two large bent clay
516 particles. Hence, it can be stated that the collapse of the larger silt adjacent pores in these mud samples is governed
517 by the bending of the clay particles and subsequent fracturing due to an increase in vertical effective stress.
518 However, all clay particles associated with larger silt-adjacent pores will not show the evidence of the bending at
519 the same point of time. The clay particles that are present within the force chain of load during compaction are
520 susceptible to exhibit bent microstructure. Nevertheless, in this study, we polished and analyzed mudstone
521 microstructure only at one plane among two equivalent counterparts. Hence, theoretically we encounter only 50%
522 of the total bent clay present in the sample.

523 Apart from large pores, small silt-adjacent pores also become less abundant with burial, but the transition occurs
524 deeper than the large pores, and small, silt-adjacent pores remain common throughout the section (Supplementary
525 data-11). Small equant pores are lost like the large pores, and elongate pores remain abundant within this
526 population subset throughout. There is a loose correspondence between the loss of small, equant pores and an
527 increase in elongate pores, suggesting that pore flattening is part of the pore collapse history. The pore collapse
528 evolution outlined for large pores (Fig.13g) appears to also hold for small pores, even though observations are
529 more challenging.

530 Small, clay domain pores appear to remain resilient throughout the compaction history (Fig. 8), even though some
531 of these pores must become lost to account for porosity loss. Small, equant pores are lost between 100-200 m, and
532 this loss appears to be accommodated by an increase in elongate pores (Fig. 8). Elongate crescent pores increase
533 in abundance around 800 mbsf, and we interpret this to reflect folding of abundant linear elongate pores as the
534 overall system compacts.

535 Large equant pores in the clay domain are lost within the first few 10's of meters of burial. Elongate pores appear
536 to form at the expense of equant pores, and there may be a reduction in pore size associated with this shape change.
537 Most of the pores remaining after 1500 m of burial are small, elongate pores found both in clay domain and silt-
538 adjacent pores.

539 The presence of silt particles locally redistributes the force chain of load to retain silt-adjacent, large pores
540 undeformed (Schneider et al., 2011). The samples with greater silt content are also enriched in equant-shaped silt-
541 adjacent larger pores (Fig.10) in the microstructure. Hence, as a result, they display greater porosity compared to
542 other samples from similar depth intervals (Fig.10).

543 As discussed earlier, previous studies report contrasting ideas on the development of phyllosilicate fabric strength
544 due to mechanical compaction. Some studies state that mechanical compaction strongly develops phyllosilicate
545 fabric in mud (Bowles et al., 1969; Oertel and Curtis, 1972; Vasseur et al., 1995), whereas other studies document,

546 vertical effective stress has limited impact on phyllosilicate fabric development (Ho et al., 1999; Aplin et al., 2006;
547 Day-Stirrat et al., 2008; 2011). Here, we consider preferred orientation of pore as a proxy to the alignment of
548 phyllosilicate (Hemes et al., 2013). It is observed, at the shallow depth (Unit-I), a weak preferred alignment of the
549 long axis of pores with maxima oriented obliquely to the bedding planes (Supplementary data-15), and at greater
550 depth (Unit-II and III), the longest axes of pores aligned subparallel to the bedding plane. Increase in vertical
551 effective stress below 28mbsf depth increases alignment of the preferred orientation of the longest axis of pores
552 only in small amount. Hence, it can be inferred, vertical stress appears to have limited control on the development
553 of phyllosilicate fabric strength in mud.

554 Performing laboratory experiments, and using mercury intrusion porosimetry, previous authors documented
555 evolution of pore size distribution in mud with an increase in consolidation stress (Griffiths and Joshi, 1989; 1990).
556 They conclude that the pore size distribution commonly appears to be bi-modal in nature, and the distribution
557 curve shifts toward smaller pore sizes with an increase in applied consolidation stress (Griffiths and Joshi, 1989).
558 However, we observe contrastingly a sharp transition from tri-modal to bi-modal pore size distribution around
559 28mbsf depth due to rapid collapse of large clay domain pores by compactional strain. With an increase in depth
560 below 28mbsf, bi-modal pore size distribution persists and tends to shift toward small pore sizes due to reduction
561 in number of larger silt-adjacent pores.

562 Previous laboratory studies have emphasized the importance of clay particle rotation as a dominant mechanism for
563 mechanical compaction in mudstone (Bennett et al., 1981, 1991; Vasseur et al., 1995; Aplin et al., 2006; Day-
564 Stirrat et al., 2008; 2011). While we observe rotation is an important mechanism for mechanical compaction at the
565 shallowest depth where unstable EE and EF particle contacts are present. Clay particle bending and
566 sliding/fracturing are considered more important for most of the section studied.

567 Mechanical compaction of marine sediment: a conceptual model

568 According to earlier studies (Delage and Lefebvre, 1884; Griffiths and Joshi, 1989; 1990; Emmanuel and Day-
569 Stirrat 2012), the reduction of pores in sedimentary rocks during compaction is size-dependent; larger pores deform
570 much readily than smaller pores. According to their model, larger pores rapidly decrease in size during compaction
571 to reduce the overall porosity of the sample. However, microstructural analysis of Sumatra samples suggests that
572 porosity reduction is accomplished by compaction of all pore sizes. Moreover, the maximum size of pores remains
573 almost constant irrespective of increasing vertical effective stress/depth (Supplementary data-8) with little
574 difference observed for the maximum pore size in samples from 98.25 mbsf and 1299.31 mbsf. The preservation
575 of a constant ratio between MAD and BIB-SEM porosity measurements (Fig. 3b) suggests that porosity loss is
576 distributed across all pore sizes. We infer that all pore sizes are available for compaction for every increment of
577 applied stress but acknowledge that pore size reduction in different size classes may proceed at different rates.

578 We propose a new model for the reduction in porosity in which all pores within the force chain of load take part
579 in the reduction of porosity during compaction irrespective of their size. At shallow depth up to 28mbsf, larger
580 clay-domain pores are the most susceptible to early response during an increase in compactional strain, because of
581 two reasons: 1) the 'domains' defined by the clay particles are weaker compared to the larger, rigid silt grains, and

582 2) due to higher relative proportion of clay-rich regions within the mud, the force chain of load dominantly passes
583 through the clay domains. The dispersed nature of the silt-size particles and the high proportion of phyllosilicates
584 in the mud samples indicate that soft clay particles act as the principal load-bearing framework. Hence, larger clay
585 domain pores are more unstable compared to silt-adjacent pores in the mud microstructure. Similarly, below
586 28mbsf depth, under an increase in vertical effective stress, both the larger silt-adjacent pores and smaller pores in
587 the clay matrix that come within the force chain of load collapse. Hence, the ratio between BIB-SEM porosity vs
588 MAD porosity remains almost constant irrespective of the depth. All larger silt-adjacent pores do not come within
589 the force chain of load at the same time. Hence, some of the larger silt-adjacent pores remained undeformed to the
590 maximum depth of 1500mbsf depth. Therefore, the maximum size of the larger silt-adjacent pores remains almost
591 constant irrespective of the depth/vertical effective stress.

592 While our understanding of how different pore types is consistent with all available data, tracking the pore
593 evolution through additional size categories would elucidate the pore evolution in more detail. Preliminary pore
594 size distribution data (Fig.9) indicate that 4 size bins exist in these samples. Developing this approach requires
595 improved image analysis techniques to tie all the pore attributes together on a pore-by-pore basis for a huge number
596 of pores.

597 [Compaction strain accommodation and grain-scale deformation](#)

598 Deformation of clay-rich sedimentary rocks involves four possible mechanisms: 1) Particulate flow; (Morgenstern
599 and Tchalenko, 1967; Borradaile et al., 1981); 2) Cataclasis; (Ukar and Cloos, 2019) 3) Diffusive mass transfer;
600 (Blenkinsop, 2007; Fossen, 2016); 4) Intercrystalline plasticity (Blenkinsop, 2007; Fossen, 2016). Intensity and
601 occurrence of a particular deformation mechanism in a mudstone depend on several parameters, such as effective
602 stress, water content, cementation, temperature (Desbois et al., 2017; Den Hartog and Spiers, 2014).

603 All our samples show evidence of particulate flow controlled by friction between grains. At shallow depths, illite
604 platelets contacted at EE and EF junctions lose these weak bonds, and particles rotate into bedding-parallel
605 orientation. Once FF contacts dominate, large-scale rotations are reduced and **intra-particle slip** becomes
606 important. This is best evidenced in collapse of large, silt-adjacent pores where bent clay particles overlie pores
607 (Fig.14a to f). In deforming granular foam material, bending was reported as the dominant deformation mechanism
608 for the reduction in porosity and developing preferred alignment of the long axis of pores perpendicular to the
609 applied stress (Elliott et al., 2002, Zhou et al., 2004; Samsudin et al., 2017; Zakaria et al., 2018) (**review of these
610 earlier studies on the experimental deformation of granular foam is described in supplementary data-17**). Friction
611 adheres clay particles to the edge of pores while the middle of particles drops into the pore, resulting in bending
612 by **intra-particle slip**. A cartoon (Fig.14g) illustrates the compaction mechanism associated with the bending of
613 clay particles. With increasing compaction strain, clay particles undergo bending, and as a result, pore area reduces
614 and the orientation of the pores tends to align perpendicular to the applied effective stress (Fig.14g). **At the shallow
615 depth (Unit-I), due to greater porosity, particles get enough free space for rotation to align parallel to the bedding
616 plane (Supplementary data-18a and b). However, at greater depth, as porosity decreases, space problem arises
617 which causes particles to deform by bending and subsequently fracturing with increase in compactional strain
618 (Supplementary data-18c and d).**

619 Compaction of Sumatra input section: generalized implication for rock property 620 evolution

621 The overall compaction curve obtained for Sumatra muds is comparable with the experimental study by Fawad et
622 al., 2010 in the context of compactional range (Fig.8). The curve shows a monoexponential decrease in porosity
623 with an increase in vertical effective stress, which is evidence of normal consolidation (Fawad et al., 2010;
624 Dutilleul et al., 2020).

625 The larger silt-adjacent pores seen in the deepest of these samples (1500 m burial) suggest these muds retain
626 considerable potential for additional **mechanical** compaction in deeper burial. As this marine sediment
627 progressively approaches greater burial at closer proximity **to** the accretionary prism, it will undergo further change
628 in physical and deformational properties (Bray and Karig, 1985). Despite the substantial compactional strain, the
629 relatively high porosity of the deepest sample and the survival of larger and mechanically unstable silt-margin
630 pores suggests that compactional stabilization has not been reached because such IGVs and pore types are not
631 generally observed in older and lithified mudrocks. Based on the current understanding of subduction zone
632 deformation behavior and mudrock properties, it seems likely that **mechanical** compaction will continue to
633 dominate the pore loss in deeper burial.

634 The general absence of early cementation and the corresponding dominance of compaction in the total pore loss,
635 is consistent with observations of other siliciclastic-dominated muds (Milliken, 2014; 2019). The trends for
636 intergranular volume **change** observed **from** the seafloor **and** 1500mbsf place useful constraints on the maximum
637 cement volumes that theoretically could be emplaced at this depth range in sediments containing a more reactive
638 grain assemblage. At the depths of burial attained at the deformation front, any cementation of the Sumatra input
639 sediments will be limited to <30% of the rock volume, or possibly much less, as **mechanical** compaction is
640 expected to continue up to the burial temperatures that initiate grain reactions and associated cementation.

641 Conclusions

642 Pores can be classified by size and also microstructural position. Their contribution to the total porosity is
643 multimodal.

644 Samples at shallow depth (seafloor to 28 mbsf) display a sharp reduction in porosity from 80% to 52% due to the
645 collapse of the large clay domain/matrix pores. Deeper samples (28 mbsf to 1500 mbsf) exhibit a smaller reduction
646 in porosity from 50% to 32% due to collapse of silt-adjacent pores by bending and subsequently fracturing/sliding
647 of clay particles.

648 The class of large pores next to silt-sized **d** grains (between 10^4 and 10^6 nm²) remains common to >1 km burial,
649 irrespective of the mineralogy of the silt-sized grains, but their size decreases with depth. Small, equant pores next
650 to silt particles are abundant in the first 100 m of burial and remain common over the whole samples depth range.

651 Small pores in clay domains are almost all elongated, and abundant over all observed depths. Small, crescent-
652 shaped elongate pores increase in abundance with depth as clay particles become folded by compaction
653 processes.

654 The size-independence of pore loss arises, because the force chain driving pore collapse is localized primarily
655 within the volumetrically dominant and weaker clay-rich domains; larger pores around isolated silt particles enter
656 into the force chain somewhat randomly and asynchronously and do not contribute preferentially to pore loss over
657 the depth range studied.

658 An increase in effective stress up to 18MPa (~1500 mbsf) causes the development of weakly aligned phyllosilicate
659 fabric (defined by mica and illite clay particles) in the microstructure.

660 Compaction processes in our samples are dominated by granular flow (rotation and frictional sliding of illite clay
661 particles) at shallow depths. With increasing depth, compaction is additionally accommodated by bending of clay
662 particles.

663 Data availability

664 High resolution SE2 and BSE images of all samples are available online at:
665 <https://figshare.com/s/cbaada517b0b1409d575>

666 Authors contributions

667 SL and KLM performed sample preparation and BIB-SEM microscopy. SL analysed the data. JLU and GD
668 acquired funding. JLU managed the project. PV, KLM and JLU significantly contributed to interpret the data. SL
669 wrote the first draft of the manuscript. PV, KLM and JLU contributed for the correction and improvement of the
670 manuscript.

671 Competing interests

672 The authors declare that they do not have any conflict of interest.

673 Acknowledgments

674 SL and JLU thank German Research Foundation (Deutsche Forschungsgemeinschaft [DFG] grant UR 64/19-1)
675 for providing funding to carry out the research. IODP (International Ocean Discovery Programme) sample
676 repository, Japan is acknowledged for providing oriented mud samples for the study. KLM acknowledges the
677 samples and data provided by the International Ocean Discovery Program (IODP). Funding for sample preparation
678 and SEM imaging was supported by a post-expedition award (Milliken, P.I.) from the Consortium for Ocean
679 Leadership. SL thanks Manuel Menzel, Jop Klaver, Liene Spruženiece, and Joyce Schmatz for providing valuable
680 time to teach BIB-SEM techniques. We would like to thank Dave Duehurst and Bernhard Schuck for their
681 constructive ideas in the review reports, and Virginia Toy for editorial handling.

682 References

- 683 Adams, R. and Bischof, L.: Seeded region growing. *IEEE Transactions on pattern analysis and machine*
684 *intelligence*. IEEE: 16(6), 641-647. [https://DOI. 10.1109/34.295913](https://doi.org/10.1109/34.295913), 1994.
- 685 Ajdukiewicz, J. M. and Lander, R. H.: Sandstone reservoir quality prediction: state of the art, *AAPG Bulletin*, 94, :
686 1082-1091, [https:// doi.org/10.1306/intro060110](https://doi.org/10.1306/intro060110), 2010.
- 687 Ammon, C.J., Ji, C., Thio, H.K., Robinson, D., Ni, S., Hjorleifsdottir, V., Kanamori, H., Lay, T., Das, S.,
688 Helmberger, D. and Ichinose, G. Rupture process of the 2004 Sumatra-Andaman earthquake, *Science*, 308(5725),
689 1133-1139, DOI: 10.1126/science.1112260, 2005.
- 690 Aplin, A.C. and Macquaker, J.H.: Mudstone diversity: Origin and implications for source, seal, and reservoir
691 properties in petroleum systems, *AAPG bulletin*, 95(12), 2031-2059, <https://doi.org/10.1306/03281110162>, 2011.
- 692 Aplin, A.C., Matenaar, I.F. and Vvan Dder Pluijm, B.A.: Influence of mechanical compaction and chemical
693 diagenesis on the microfabric and fluid flow properties of Gulf of Mexico mudstones *Journal of Geochemical*
694 *Exploration*, 78, 449-451, [https://doi.org/10.1016/S0375-6742\(03\)00035-9](https://doi.org/10.1016/S0375-6742(03)00035-9), 2003.
- 695 Aplin, A.C., Matenaar, I.F., McCarty, D.K. and Vvan Der Pluijm, B.A.: Influence of mechanical compaction and
696 clay mineral diagenesis on the microfabric and pore-scale properties of deep-water Gulf of Mexico mudstones,
697 *Clays and Clay Minerals*, 54(4), 500-514, <https://doi.org/10.1346/CCMN.2006.0540411>, 2006.
- 698 Backman, J., Chen, W., Kachovich, S., Mitchison, F. L., Petronotis, K. E., Yang, T. and Zhao, X.: Data report:
699 Revised age models for IODP Sites U1480 and U1481, Expedition 362, *Proceedings of the International Ocean*
700 *Discovery Program, Expedition Reports 362*, <https://doi.org/10.14379/iodp.proc.362.202.2019>, 2019.
- 701 Baruch, E.T., Kennedy, M.J., Löhr, S.C. and Dewhurst, D.N.: Feldspar dissolution-enhanced porosity in
702 Paleoproterozoic shale reservoir facies from the Barney Creek Formation (McArthur Basin, Australia). *AAPG*
703 *Bulletin*, 99(9), 1745-1770, <https://doi.org/10.1306/04061514181>, 2015.
- 704 Bennett, R.H., Bryant, W.R. and Keller, G.H.: Clay fabric of selected submarine sediments; fundamental properties
705 and models, *Journal of Sedimentary Research*, 51(1), 217-232, [https://doi.org/10.1306/212F7C52-2B24-11D7-](https://doi.org/10.1306/212F7C52-2B24-11D7-8648000102C1865D)
706 [8648000102C1865D](https://doi.org/10.1306/212F7C52-2B24-11D7-8648000102C1865D), 1981.
- 707 Bennett, R.H., O'Brien, N.R. and Hulbert, M.H.: Determinants of clay and shale microfabric signatures: processes
708 and mechanisms. In *Microstructure of Fine-Grained Sediments*, 5-32, Springer, New York, NY. [https://DOI:](https://DOI:10.1007/978-1-4612-4428-8_2)
709 [10.1007/978-1-4612-4428-8_2](https://DOI:10.1007/978-1-4612-4428-8_2), 1991.
- 710 Blenkinsop, T.G.: *Deformation microstructures and mechanisms in minerals and rocks*, Springer Science &
711 *Business Media*, 2007.

712 Bowles, F.A., Bryant, W.R. and Wallin, C.: Microstructure of unconsolidated and consolidated marine sediments,
713 Journal of Sedimentary Research, 39(4), 1546-1551, [https://doi.org/10.1306/74D71E7E-2B21-11D7-](https://doi.org/10.1306/74D71E7E-2B21-11D7-8648000102C1865D)
714 8648000102C1865D, 1969.

715 Borradaile, G.J.: Particulate flow of rock and the formation of cleavage. Tectonophysics, 72(3-4), 305-321,
716 [https://doi.org/10.1016/0040-1951\(81\)90243-2](https://doi.org/10.1016/0040-1951(81)90243-2), 1981.

717 Bray, C.J. and Karig, D.E.: Porosity of sediments in accretionary prisms and some implications for dewatering
718 processes, Journal of Geophysical Research: Solid Earth, 90(B1), 768-778, [https://doi.org/](https://doi.org/10.1029/JB090iB01p00768)
719 10.1029/JB090iB01p00768, 1985.

720 Brown, K.M. and Ransom, B.: Porosity corrections for smectite-rich sediments: Impact on studies of compaction,
721 fluid generation, and tectonic history. Geology, 24(9), 843-846, [https://doi.org/10.1130/0091-](https://doi.org/10.1130/0091-7613(1996)024<0843:PCFSRS>2.3.CO;2)
722 7613(1996)024<0843:PCFSRS>2.3.CO;2, 1996.

723 Burland, J.B.: On the compressibility and shear strength of natural clays. Géotechnique, 40(3), 329-378,
724 doi.org/10.1680/geot.1990.40.3.329, 1990.

725 Chester, F.M., Rowe, C., Ujiie, K., Kirkpatrick, J., Regalla, C., Remitti, F., Moore, J.C., Toy, V., Wolfson-
726 Schwehr, M., Bose, S. and Kameda, J.: Structure and composition of the plate-boundary slip zone for the 2011
727 Tohoku-Oki earthquake. Science, 342(6163), 1208-1211, [https://DOI: 10.1126/science.1243719](https://DOI:10.1126/science.1243719), 2013.

728 Day-Stirrat, R.J., Aplin, A.C., Środoń, J. and Van der Pluijm, B.A.: Diagenetic reorientation of phyllosilicate
729 minerals in Paleogene mudstones of the Podhale Basin, southern Poland, Clays and Clay Minerals, 56(1), 100-
730 111, DOI: 10.1346/CCMN.2008.0560109, 2008.

731 Day-Stirrat, R.J., Flemings, P.B., You, Y., Aplin, A.C. and van der Pluijm, B.A.: The fabric of consolidation in
732 Gulf of Mexico mudstones, Marine Geology, 295, 77-85, <https://doi.org/10.1016/j.margeo.2011.12.003>, 2012.

733 Day-Stirrat, R.J., Milliken, K.L., Dutton, S.P., Loucks, R.G., Hillier, S., Aplin, A.C. and Schleicher, A.M.: Open-
734 system chemical behavior in deep Wilcox Group mudstones, Texas Gulf Coast, USA, Marine and Petroleum
735 Geology, 27(9), 1804-1818, <https://doi.org/10.1016/j.marpetgeo.2010.08.006>, 2010.

736 Day-Stirrat, R.J., Schleicher, A.M., Schneider, J., Flemings, P.B., Germaine, J.T. and van der Pluijm, B.A.:
737 Preferred orientation of phyllosilicates: Effects of composition and stress on resedimented mudstone
738 microfabrics, Journal of Structural Geology, 33(9), 1347-1358, <https://DOI:10.1016/j.jsg.2011.06.007>, 2011.

739 Dean, S.M., McNeill, L.C., Henstock, T.J., Bull, J.M., Gulick, S.P., Austin, J.A., Bangs, N.L., Djajadihardja, Y.S.
740 and Permana, H.: Contrasting décollement and prism properties over the Sumatra 2004–2005 earthquake rupture
741 boundary, Science, 329(5988), 207-210, [https://DOI: 10.1126/science.1189373](https://DOI:10.1126/science.1189373), 2010.

742 Delage, P. and Lefebvre, G.: Study of the structure of a sensitive Champlain clay and of its evolution during
743 consolidation. Canadian Geotechnical Journal, 21(1), 21-35, <https://doi.org/10.1139/t84-003>, 1984.

744 Delle Piane, C., Almqvist, B.S., MacRae, C.M., Torpy, A., Mory, A.J. and Dewhurst, D.N.: Texture and diagenesis
745 of Ordovician shale from the Canning Basin, Western Australia: Implications for elastic anisotropy and
746 geomechanical properties. *Marine and Petroleum Geology*, 59, 56-71, doi.org/10.1016/j.marpetgeo.2014.07.017,
747 2015.

748 Den Hartog, S. A. and Spiers, C. J.: A microphysical model for fault gouge friction applied to subduction
749 megathrusts, *Journal of Geophysical Research: Solid Earth*, 119(2), 1510-1529.
750 <https://doi.org/10.1002/2013JB010580>, 2014.

751 Desbois, G., Urai, J.L. and Kukla, P.A.: Morphology of the pore space in claystones—evidence from BIB/FIB ion
752 beam sectioning and cryo-SEM observations. *eEarth Discussions*, 4(1), 1-19, 2009.

753 Desbois, G., Urai, J.L., Hemes, S., Brassinnes, S., De Craen, M. and Sillen, X.: Nanometer-scale pore fluid
754 distribution and drying damage in preserved clay cores from Belgian clay formations inferred by BIB-cryo-
755 SEM. *Engineering Geology*, 179, 117-131, <https://doi.org/10.1016/j.enggeo.2014.07.004>, 2014.

756 Desbois, G., Höhne, N., Urai, J. L., Bésuelle, P., and Viggiani, G.: Deformation in cemented mudrock (Callovo–
757 Oxfordian Clay) by microcracking, granular flow and phyllosilicate plasticity: insights from triaxial deformation,
758 broad ion beam polishing and scanning electron microscopy, *Solid Earth*, 8, 291–305, <https://doi.org/10.5194/se-8-291-2017>, 2017.

760 Desbois, G., Urai, J. L., Kukla, P. A., Konstanty, J., & Baerle, C.: High-resolution 3D fabric and porosity model
761 in a tight gas sandstone reservoir: A new approach to investigate microstructures from mm-to nm-scale combining
762 argon beam cross-sectioning and SEM imaging. *Journal of Petroleum Science and Engineering*, 78(2), 243-257,
763 <https://doi.org/10.1016/j.petrol.2011.06.004>, 2011.

764 Dugan, B., McNeill, L. and Petronotis, K.: Expedition 362 preliminary report: Sumatra subduction zone,
765 International Ocean Discovery Program, 2017.

766 Dutilleul, J., Bourlange, S., Conin, M. and Géraud, Y.: Quantification of bound water content, interstitial porosity
767 and fracture porosity in the sediments entering the North Sumatra subduction zone from Cation Exchange Capacity
768 and IODP Expedition 362 resistivity data, *Marine and Petroleum Geology*, 111, 156-165.,
769 <https://doi.org/10.1016/j.marpetgeo.2019.08.007>, 2020.

770 Ehrenberg, S. N.: Assessing the relative importance of compaction processes and cementation to reduction of
771 porosity in sandstones: discussion. *American Association of Petroleum Geologists Bulletin*, 73, 1274-1276,
772 <https://doi.org/10.1306/44B4AA1E-170A-11D7-8645000102C1865D>, 1989.

773 Elliott, J.A., Windle, A.H., Hobdell, J.R., Eeckhaut, G., Oldman, R.J., Ludwig, W., Boller, E., Cloetens, P. and
774 Baruchel, J.: In-situ deformation of an open-cell flexible polyurethane foam characterised by 3D computed
775 microtomography, *Journal of materials science*, 37(8), 1547-1555, doi:10.1023/A:1014920902712, 2002.

776 Emmanuel, S. and Day-Stirrat, R.J.: 2012. A framework for quantifying size dependent deformation of nano-scale
777 pores in mudrocks *Journal of applied geophysics*, 86, 29-35, <https://doi.org/10.1016/j.jappgeo.2012.07.011>, 2012.

778 Fawad, M., Mondol, N.H., Jahren, J. and Bjørlykke, K.: Microfabric and rock properties of experimentally
779 compressed silt-clay mixtures, *Marine and Petroleum Geology*, 27(8), 1698-1712,
780 <https://doi.org/10.1016/j.marpetgeo.2009.10.002>, 2010.

781 Fossen, H.: *Structural geology*. Cambridge university press. 2016.

782 Ghosal, D., Singh, S.C. and Martin, J.: Shallow subsurface morphotectonics of the NW Sumatra subduction system
783 using an integrated seismic imaging technique, *Geophysical Journal International*, 198(3), 1818-1831,
784 <https://doi.org/10.1093/gji/ggu182>, 2014.

785 Griffiths, F.J. and Joshi, R.C.: Change in pore size distribution due to consolidation of clays. *Geotechnique*, 39(1),
786 159-167, doi.org/10.1680/geot.1989.39.1.159, 1989.

787 Griffiths, F.J. and Joshi, R.C.: Clay fabric response to consolidation. *Applied clay science*, 5(1), 37-66,
788 [doi.org/10.1016/0169-1317\(90\)90005-A](https://doi.org/10.1016/0169-1317(90)90005-A), 1990.

789 Griffiths, F.J. and Joshi, R.C.: Change in pore size distribution owing to secondary consolidation of
790 clays. *Canadian Geotechnical Journal*, 28(1), 20-24, <https://doi.org/10.1139/t91-003>, 1991.

791 Hemes, S., Desbois, G., Klaver, J. and Urai, J.L.: Microstructural characterisation of the Ypresian clays (Kallo-1)
792 at nanometre resolution, using broad-ion beam milling and scanning electron microscopy. *Netherlands Journal of*
793 *Geosciences*, 95(3), 293-313, DOI: <https://doi.org/10.1017/njg.2016.16>, 2016.

794 Hemes, S., Desbois, G., Urai, J.L., De Craen, M. and Honty, M.: Variations in the morphology of porosity in the
795 Boom Clay Formation: insights from 2D high resolution BIB-SEM imaging and Mercury injection
796 Porosimetry. *Netherlands Journal of geosciences*, 92(4), 275-300, DOI: doi.org/10.1017/S0016774600000214,
797 2013.

798 Hemes, S., Desbois, G., Urai, J.L., Schröppel, B. and Schwarz, J.O.: Multi-scale characterization of porosity in
799 Boom Clay (HADES-level, Mol, Belgium) using a combination of X-ray μ -CT, 2D BIB-SEM and FIB-SEM
800 tomography. *Microporous and mesoporous materials*, 208, 1-20, [https://](https://doi.org/10.1016/j.micromeso.2015.01.022)
801 doi.org/10.1016/j.micromeso.2015.01.022, 2015.

802 Hesse, R.: Turbiditic and non-turbiditic mudstone of Cretaceous flysch sections of the East Alps and other
803 basins. *Sedimentology*, 22(3), 387-416, <https://doi.org/10.1111/j.1365-3091.1975.tb01638.x>, 1975.

804 Hippchen, S. and Hyndman, R.D.: Thermal and structural models of the Sumatra subduction zone: Implications
805 for the megathrust seismogenic zone. *Journal of Geophysical Research: Solid Earth*, 113(B12), [https://doi.org/10.](https://doi.org/10.1002/2015TC003901)
806 <https://doi.org/10.1002/2015TC003901>, 2008.

807 Ho, N.C., Peacor, D.R. and Van der Pluijm, B.A.: Preferred orientation of phyllosilicates in Gulf Coast mudstones
808 and relation to the smectite-illite transition. *Clays and Clay Minerals*, 47(4), 495-504, DOI: 10.1346/CCMN.
809 1999.0470412, 1999.

810 Houben, M.E., Desbois, G. and Urai, J.L.: A comparative study of representative 2D microstructures in Shaly and
811 Sandy facies of Opalinus Clay (Mont Terri, Switzerland) inferred from BIB-SEM and MIP methods, *Marine and*
812 *Petroleum Geology*, 49, 143-161, <https://doi.org/10.1016/j.marpetgeo.2013.10.009>,. 2014.

813 Hüpers, A., Ikari, M.J., Dugan, B., Underwood, M.B. and Kopf, A.J.: Origin of a zone of anomalously high
814 porosity in the subduction inputs to Nankai Trough. *Marine Geology*, 361, 147-162,
815 <https://doi.org/10.1016/j.margeo.2015.01.004>, 2015.

816 Hüpers, A., Torres, M.E., Owari, S., McNeill, L.C., Dugan, B., Henstock, T.J., Milliken, K.L., Petronotis, K.E.,
817 Backman, J., Bourlange, S. and Chemale, F.: Release of mineral-bound water prior to subduction tied to shallow
818 seismogenic slip off Sumatra. *Science*, 356(6340), 841-844. 2017.

819 Jiang, M., Klaver, J., Schmatz, J. and Urai, J.L.: Nanoscale porosity analysis in geological materials. *Acta*
820 *Stereologica*, 2015.

821 Kameda, A., Dvorkin, J., Keehm, Y., Nur, A. and Bosl, W.: Permeability-porosity transforms from small sandstone
822 fragments. *Geophysics*, 71(1), N11-N19, <https://doi.org/10.1190/1.2159054>, 2006.

823 Karaborni, S., Smit, B., Heidug, W., Urai, J. and Van Oort, E.: The swelling of clays: molecular simulations of
824 the hydration of montmorillonite. *Science*, 271(5252), 1102-1104, DOI: 10.1126/science.271.5252.1102, 1996.

825 Klaver, J., Desbois, G., Littke, R. and Urai, J.L.: BIB-SEM characterization of pore space morphology and
826 distribution in postmature to overmature samples from the Haynesville and Bossier Shales. *Marine and petroleum*
827 *Geology*, 59, 451-466, <https://doi.org/10.1016/j.marpetgeo.2014.09.020>, 2015.

828 Klaver, J., Desbois, G., Littke, R. and Urai, J.L.: BIB-SEM pore characterization of mature and post mature
829 Posidonia Shale samples from the Hils area, Germany. *International Journal of Coal Geology*, 158, 78-89,
830 <https://doi.org/10.1016/j.coal.2016.03.003>, 2016.

831 Klaver, J., Desbois, G., Urai, J.L. and Littke, R.: BIB-SEM study of the pore space morphology in early mature
832 Posidonia Shale from the Hils area, Germany. *International Journal of Coal Geology*, 103, 12-25.
833 <https://doi.org/10.1016/j.coal.2012.06.012>, 2012.

834 Kuila, U. and Prasad, M.: Specific surface area and pore-size distribution in clays and shales. *Geophysical*
835 *Prospecting*, 61(2-Rock Physics for Reservoir Exploration, Characterisation and Monitoring), pp.341-362,
836 <https://doi.org/10.1111/1365-2478.12028>, 2013.

837 Lander, R. H. and Walderhaug, O. W.: Predicting porosity through simulating sandstone compaction and quartz
838 cementation. American Association of Petroleum Geologists Bulletin 83: 433-449,
839 <https://doi.org/10.1306/00AA9BC4-1730-11D7-8645000102C1865D>, 1999.

840 Lander, R. H., Larese, R. H. Larese and Bonnell, L. M.: Toward more accurate quartz cement models: The
841 importance of euhedral versus noneuhedral growth rates. American Association Petroleum Geologists Bulletin 92:
842 1537-1563. <https://doi.org/10.1306/07160808037>, 2008.

843 Laurich, B., Urai, J.L., Desbois, G., Vollmer, C. and Nussbaum, C.: Microstructural evolution of an incipient fault
844 zone in Opalinus Clay: Insights from an optical and electron microscopic study of ion-beam polished samples from
845 the Main Fault in the Mt-Terri Underground Research Laboratory. Journal of Structural Geology, 67, 107-128.
846 <https://doi.org/10.1016/j.jsg.2014.07.014>, 2014.

847 Lay, T., Kanamori, H., Ammon, C. J., Nettles, M., Ward, S.N., Aster, R.C., Beck, S.L., Bilek, S.L., Brudzinski,
848 M.R., Butler, R. and DeShon, H.R.: The great Sumatra-Andaman earthquake of 26 Ddecember
849 2004. Sscience, 308(5725), pp.1127-1133, DOI: 10.1126/science.1112250, 2005.

850 Lazar, O.R., Bohacs, K.M., Macquaker, J.H., Schieber, J. and Demko, T.M.: Capturing key attributes of fine-
851 grained sedimentary rocks in outcrops, cores, and thin sections: nomenclature and description guidelines. Journal
852 of Sedimentary Research, 85(3), pp.230-246, <https://doi.org/10.2110/jsr.2015.11>, 2015.

853 Lundegard, P. D.: Sandstone porosity loss--a 'big picture' view of the importance of compaction. Journal of
854 Sedimentary Petrology 62: 250-260, <https://doi.org/10.1306/D42678D4-2B26-11D7-8648000102C1865D>, 1992.

855 McNeill, L.C., Dugan, B. and Petronotis, K.E.: Sumatra Subduction Zone. Proceedings of the International Ocean
856 Discovery Program, 362, <https://doi.org/10.14379/iodp.proc.362.102.2017>, 2017.

857 Meade, R.H.: Removal of water and rearrangement of particles during the compaction of clayey sediments. US
858 Government Printing Office, 1964.

859 Mesri, G. and Olson, R.E.: Mechanisms controlling the permeability of clays. Clays and Clay minerals, 19(3),
860 151-158, 1971.

861 Milliken, K. L.: A compositional classification for grain assemblages in fine-grained sediments and sedimentary
862 rocks. Journal of Sedimentary Research 84: 1185-1199, <https://doi.org/10.2110/jsr.2014.92>, 2008.

863 Milliken, K. L.: A compositional classification for grain assemblages in fine-grained sediments and sedimentary
864 rocks. Journal of Sedimentary Research 84: 1185-1199, <https://doi.org/10.2110/jsr.2014.92>, 2014.

865 Milliken K. L.: Compactional and mass-balance constraints inferred from the volume of quartz cementation in
866 mudrocks. Mudstone Diagenesis: New Research Perspectives for Shale Hydrocarbon Reservoirs, Seals, and
867 Source Rocks. AAPG. 120: 33-48, DOI: 10.1306/13672209M121252, 2019.

868 Milliken, K. L. and Curtis, M. E.: Imaging pores in sedimentary rocks: Foundation of porosity prediction. *Marine*
869 *and Petroleum Geology* 73,: 590-608, <https://doi.org/10.1016/j.marpetgeo.2016.03.020>, 2016.

870 Milliken, K. L. and Day-Stirrat R. J.: Cementation in mudrocks: Brief review with examples from cratonic basin
871 mudrocks. *Memoir. J.-Y. Chatellier*. Tulsa, Oklahoma, USA, AAPG, <https://doi.org/10.1306/13401729H55252>,
872 2013.

873 Milliken, K. L. and Olson, T.: Silica diagenesis, porosity evolution, and mechanical behavior in siliceous
874 mudstones, Mowry Shale Cretaceous, Rocky Mountains, U.S.A. *Journal of Sedimentary Research* 87: 366-387,
875 [.https://doi.org/10.2110/jsr.2017.24](https://doi.org/10.2110/jsr.2017.24), 2017.

876 Milliken, K. L., Rudnicki, M., Awwiller, D. N. and Zhang, T.: Organic matter-hosted pore system, Marcellus
877 Formation Devonian, Pennsylvania, USA. *AAPG Bulletin* 97: 177-200, <https://doi.org/10.1306/07231212048>,
878 2013.

879 Milliken, K. L., Esch, W. L., Reed, R. M. and Zhang, T.: Grain assemblages and strong diagenetic overprinting
880 in siliceous mudrocks, Barnett Shale Mississippian, Fort Worth Basin, Texas, U.S.A. *AAPG Bulletin* 96: 1553-
881 1578, <https://doi.org/10.1306/12011111129>, 2012.

882 Mitchell, J.K.: The fabric of natural clays and its relation to engineering properties. In *Highway Research Board*
883 *Proceedings*, 35, 1956.

884 Moeremans, R.E. and Singh, S.C.: Fore-arc basin deformation in the Andaman-Nicobar segment of the Sumatra-
885 Andaman subduction zone: Insight from high-resolution seismic reflection data, *Tectonics*, 34(8), 1736-1750,
886 doi.org/10.1002/2015TC003901, 2015.

887 Mondol, N.H., Bjørlykke, K., Jahren, J. and Høeg, K.: Experimental mechanical compaction of clay mineral
888 aggregates—Changes in physical properties of mudstones during burial. *Marine and petroleum geology*, 24(5),
889 289-311, <https://doi.org/10.1016/j.marpetgeo.2007.03.006>, 2007.

890 Morgenstern, N.R. and Tchalenko, J.S.: Microstructural observations on shear zones from slips in natural clays,
891 1967.

892 Nakano, R.: On weathering and change of properties of tertiary mudstone related to landslide. *Soils and*
893 *Foundations*, 7(1), 1-14, <https://doi.org/10.3208/sandf1960.7.1>, 1967.

894 Neagu, R.C., Cartwright, J. and Davies, R.: Measurement of diagenetic compaction strain from quantitative
895 analysis of fault plane dip. *Journal of Structural Geology*, 32(5), 641-655,
896 <https://doi.org/10.1016/j.jsg.2010.03.010>, 2010.

897 Nole, M., Daigle, H., Milliken, K.L. and Prodanović, M.: A method for estimating microporosity of fine-grained
898 sediments and sedimentary rocks via scanning electron microscope image analysis. *Sedimentology*, 63(6), 1507-
899 1521, <https://doi.org/10.1111/sed.12271>, 2016.

900 Nollet, S., Hilgers, C. and Urai, J.: Sealing of fluid pathways in overpressure cells: a case study from the
901 Buntsandstein in the Lower Saxony Basin (NW Germany). *International Journal of Earth Sciences*, 94(5), 1039-
902 1055, <https://doi.org/10.1007/s00531-005-0492-1>, 2005.

903 Oelker, A.: Deformation properties of Boom Clay: Implementation of a multi-scale concept. Dissertation,
904 Rheinisch-Westfälische Technische Hochschule Aachen, DOI: 10.18154/RWTH-2019-09913, 2019.

905 Oertel, G. and Curtis, C.D.: Clay-ironstone concretion preserving fabrics due to progressive
906 compaction. *Geological Society of America Bulletin*, 83(9), 2597-2606, [https://doi.org/10.1130/0016-7606\(1972\)83\[2597:CCPFD\]2.0.CO;2](https://doi.org/10.1130/0016-7606(1972)83[2597:CCPFD]2.0.CO;2), 1972.

908 Paxton, S. T., J. O. Szabo, J. M. Adjukiewicz and R. E. Klimentidis.: Construction of an intergranular volume
909 compaction curve for evaluating and predicting compaction and porosity loss in rigid-grain sandstone reservoirs.
910 *American Association of Petroleum Geologists Bulletin* 86: 2047-2067, <https://doi.org/10.1306/61EEDDFA-173E-11D7-8645000102C1865D>, 2002.

912 Pickering, K.T., Carter, A., Andò, S., Garzanti, E., Limonta, M., Vezzoli, G. and Milliken, K.L.: 2020. Deciphering
913 relationships between the Nicobar and Bengal submarine fans, Indian Ocean. *Earth and Planetary Science*
914 *Letters*, 544, 116329, <https://doi.org/10.1016/j.epsl.2020.116329>, 2020.

915 Pommer, M. E. and Milliken, K. L.: Pore types and pore-size distributions across thermal maturity, Eagle Ford
916 Formation, South Texas. *AAPG Bulletin* 99: 1713-1744, <https://doi.org/10.1306/03051514151>, 2015.

917 Prawirodirdjo, L., Boel, Y., McCaffrey, R., Genrich, J., Calais, E., Stevens, C., Puntodewo, S.S.O., Subarya, C.,
918 Rais, J., Zwick, P. and Fauzi, R.M.: Geodetic observations of interseismic strain segmentation at the Sumatra
919 subduction zone. *Geophysical research letters*, 24(21), 2601-2604, <https://doi.org/10.1029/97GL52691>, 1997.

920 Rieke, H.H. and Chilingarian, G.V.: *Compaction of argillaceous sediments*. Elsevier, 1974.

921 Rosenberger, K., Underwood, M.B., Vrolijk, P. and Haines, S.: Data report: clay mineral assemblages in
922 hemipelagic sediments entering the Sumatra subduction zone, IODP Sites U1480 and U1481, Expedition
923 362. *Expedition*, 362, 1. 2020.

924 Samsudin, M.S.F., Ariff, Z.M. and Ariffin, A.: Deformation behavior of open-cell dry natural rubber foam: Effect
925 of different concentration of blowing agent and compression strain rate. In *AIP Conference Proceedings*, 1835,
926 No. 1, 020007, AIP Publishing LLC, 2017.

927 Schmatz, J., Klaver, J., Jiang, M. and Urai, J.L.: Nanoscale morphology of brine/oil/mineral contacts in connected
928 pores of carbonate reservoirs: Insights on wettability from Cryo-BIB-SEM. *SPE Journal*, 22(05), 1374-1384,
929 <https://doi.org/10.2118/180049-PA>, 2017.

930 Schneider, J., Flemings, P.B., Day-Stirrat, R.J. and Germaine, J.T.: Insights into pore-scale controls on mudstone
931 permeability through resedimentation experiments. *Geology*, 39(11), 1011-1014,
932 <https://doi.org/10.1130/G32475.1> , 2011.

933 Sintubin, M.: Clay fabrics in relation to the burial history of shales. *Sedimentology*, 41(6), 1161-1169,
934 <https://doi.org/10.1130/G32475.1>, 1994.

935 Terzaghi, K. and Peck, R.B.: *Soil Mechanics. Engineering Practice*. John Wiley and Sons, Inc., New York, 1948.

936 Torres, M. E., Milliken, K. L., A. Hüpers, J. H. Kim, S. G. Lee: Authigenic clays versus carbonate formation as
937 products of marine silicate weathering in the input sequence to the Sumatra Subduction Zone, *Gechemistry,*
938 *Geophysics Geosystems*, 23 (4), <https://doi.org/10.1029/2022GC010338>, 2022.

939 Ukar, E. and Cloos, M.: Cataclastic deformation and metasomatism in the subduction zone of mafic blocks-in-
940 mélange, San Simeon, California, *Lithos*, 346, 105116, <https://doi.org/10.1016/j.lithos.2019.06.018>, 2019.

941 Vasseur, G., Djeran-Maigre, I., Grunberger, D., Rousset, G., Tessier, D. and Velde, B.: Evolution of structural and
942 physical parameters of clays during experimental compaction, *Marine and petroleum geology*, 12(8), pp.941-954,
943 [https://doi.org/10.1016/0264-8172\(95\)98857-2](https://doi.org/10.1016/0264-8172(95)98857-2), 1995.

944 Velde, B.: Compaction trends of clay-rich deep sea sediments, *Marine Geology* 133(3-4): 193-201,
945 [https://doi.org/10.1016/0025-3227\(96\)00020-5](https://doi.org/10.1016/0025-3227(96)00020-5), 1996.

946 Vrolijk, P.: On the mechanical role of smectite in subduction zones. *Geology*, 18(8), pp.703-707,
947 [https://doi.org/10.1130/0091-7613\(1990\)018<0703:OTMROS>2.3.CO;2](https://doi.org/10.1130/0091-7613(1990)018<0703:OTMROS>2.3.CO;2), 1990.

948 Wang, X., Jiang, Z., Jiang, S., Chang, J., Zhu, L., Li, X. and Li, J.: Full-scale pore structure and fractal dimension
949 of the Longmaxi shale from the Southern Sichuan Basin: Investigations using FE-SEM, gas adsorption and
950 mercury intrusion porosimetry. *Minerals*, 9(9), p.543, <https://doi.org/10.3390/min9090543>, 2019.

951 Yagiz, S.: Overview of classification and engineering properties of shales for design considerations.
952 *In Construction and Materials Issues* 2001, 156-165, 2001.

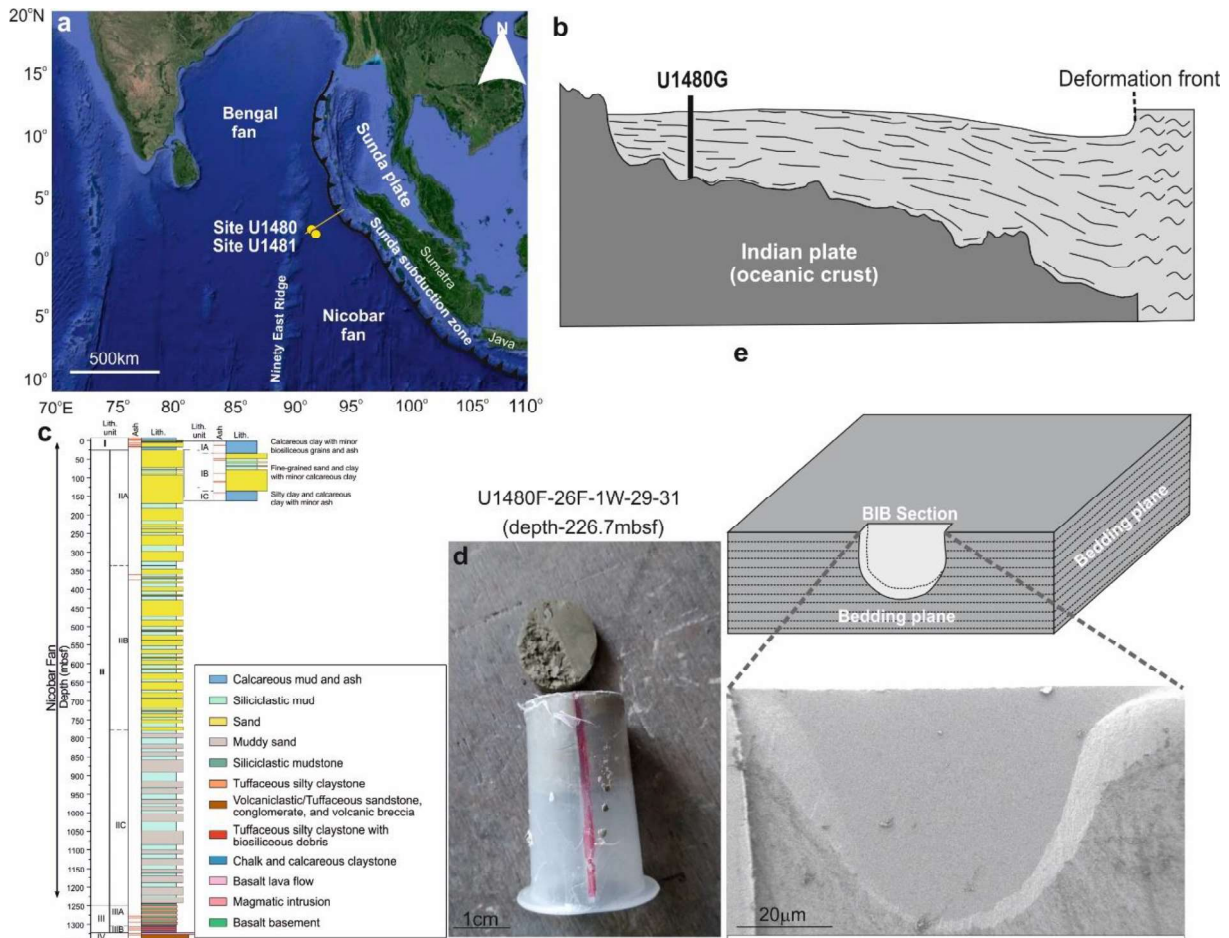
953 Zakaria, Z., Mohamad Ariff, Z. and Abu Bakar, A.: Monitoring deformation mechanism of foam cells in
954 polyethylene foams via optical microscopy: Effect of density and microstructure. *Journal of Cellular*
955 *Plastics*, 54(6), 957-976, <https://doi.org/10.1177/0021955X18795035>, 2018.

956 Zhou, J., Shrotriya, P. and Soboyejo, W.O.: Mechanisms and mechanics of compressive deformation in open-cell
957 Al foams. *Mechanics of Materials*, 36(8), 781-797, <https://doi.org/10.1016/j.mechmat.2003.05.004>,. 2004.

958

959

960



961

962 **Fig.1:** (a) **Satellite image** of Sumatra subduction zone and location of U1480 and U1481 drilling sites (created
963 from Google Maps). (b) **Schematic diagram representing location of drilling site and one of the drill holes (hole**
964 **G) at site U1480 in sectional view** (adapted from seismic profile after Hüpers et al., 2017). **The location and**
965 **extension of the seismic profile is represented by red line in (a).** (c) Lithostratigraphic units encountered at Site
966 U1480 (adapted after McNeill et al., 2017). (d) Representative tube sample received from IODP repository, Japan.
967 Red-colored line on tube surface represents notch used to denote orientation of samples collected from drill core.
968 (e) Representative BIB cross-section polished perpendicular to bedding planes.

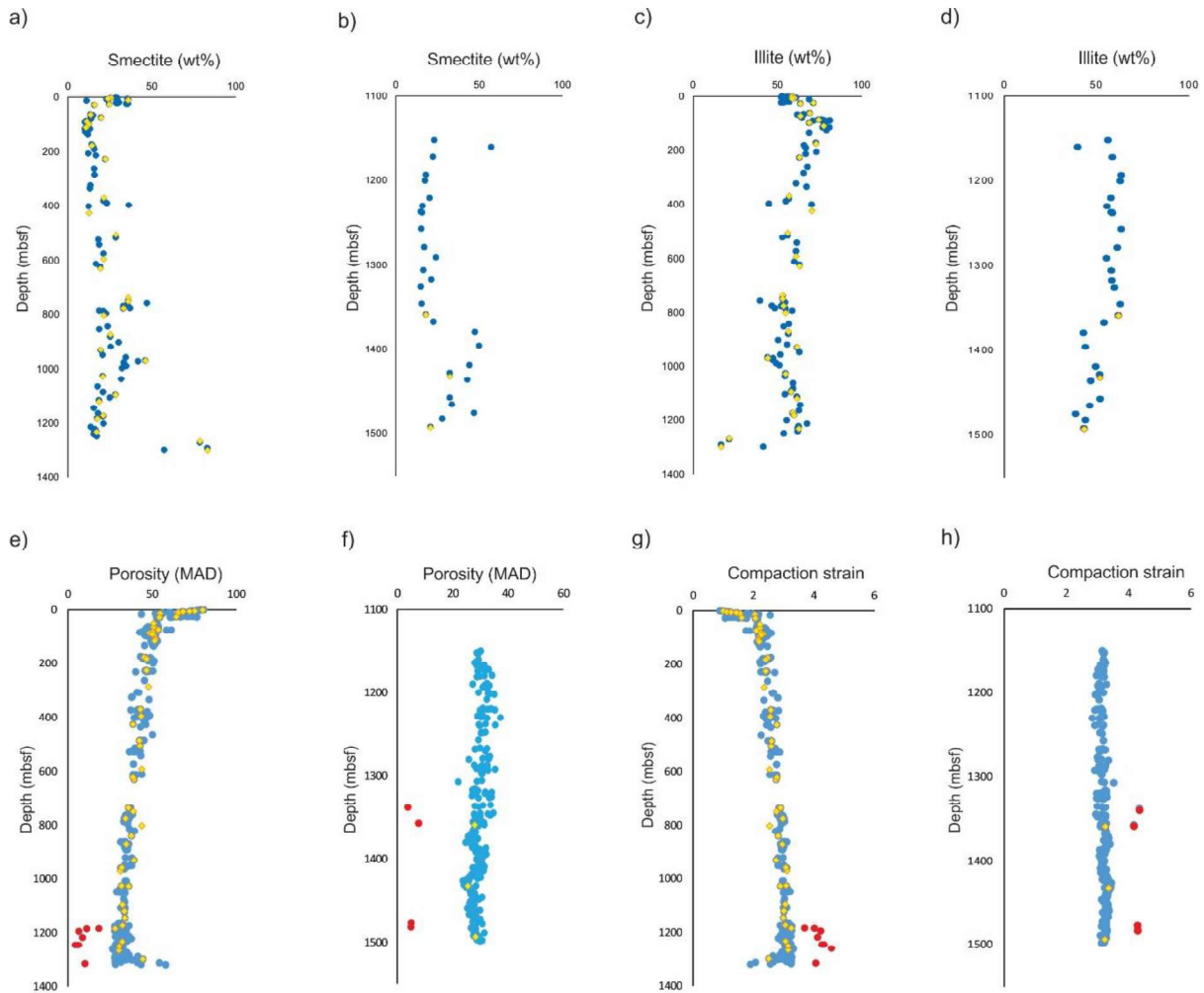
969

970

971

972

973



975

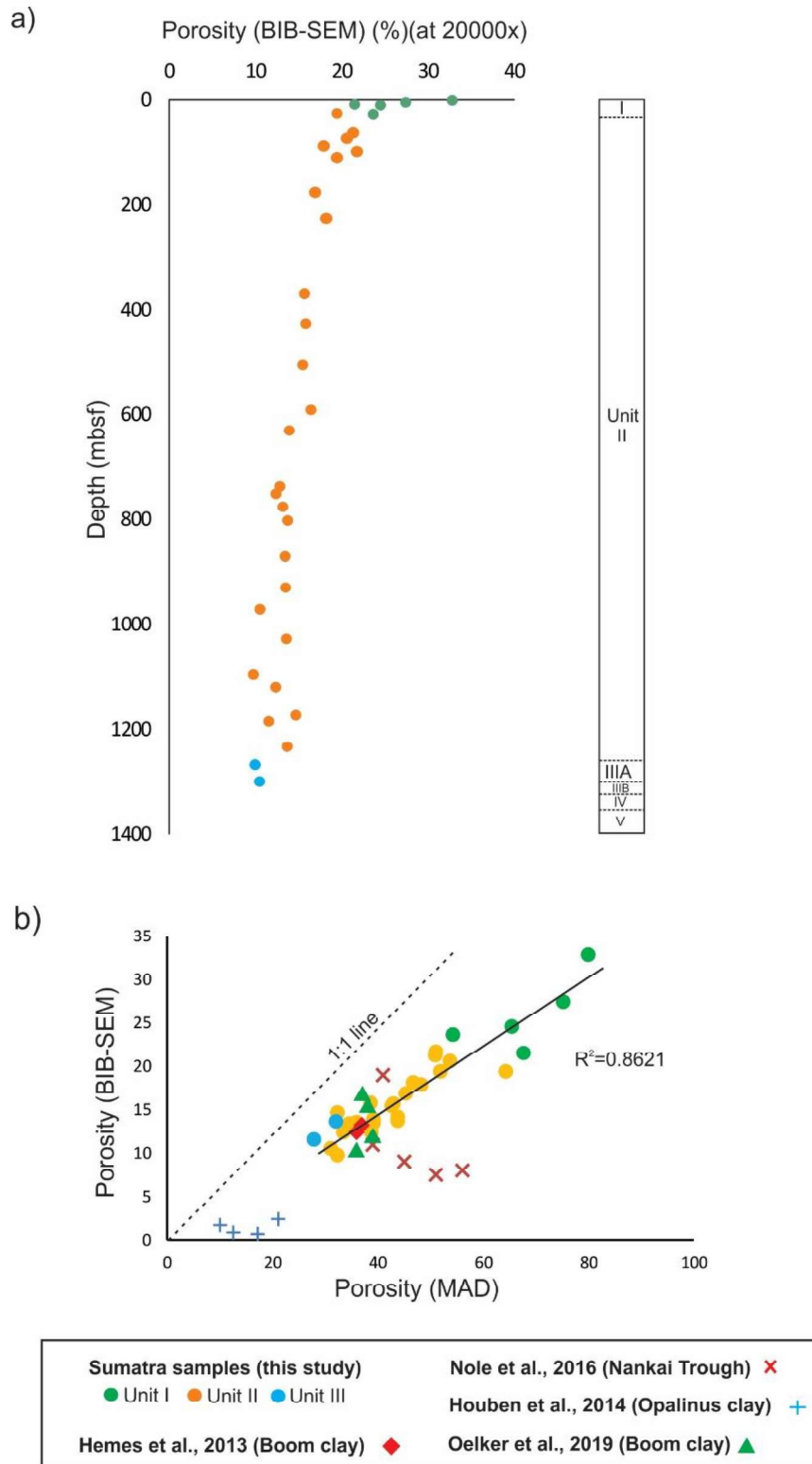
976 **Fig.2:** (a) and (b) Depth vs smectite content (wt%) for the samples from the site U1480 and U1481 respectively
 977 (blue symbol). (c) and (d) show cross-plot diagrams for depth vs Illite content (wt%) for the analysed samples
 978 from U1480 and U1481 drilling sites (blue symbol). (e) and (f) Shipboard MAD (Moisture and density) porosity
 979 vs depth data for mudstone samples recovered from Sites U1480 and U1481 (blue symbol); (g) and (h) Cross-plot
 980 diagrams for estimated compaction strain vs depth corresponding to samples recovered from Sites U1480 and
 981 U1481 (blue symbols). Yellow-colored symbols in (a), (b), (c), (d), (e), (f), (g) and (h) show 55 mud samples
 982 analyzed at RWTH-Aachen and BEG using Ar-ion milling and SEM imaging in the present study. Red-colored
 983 points are cemented (concretion) samples.

984

985

986

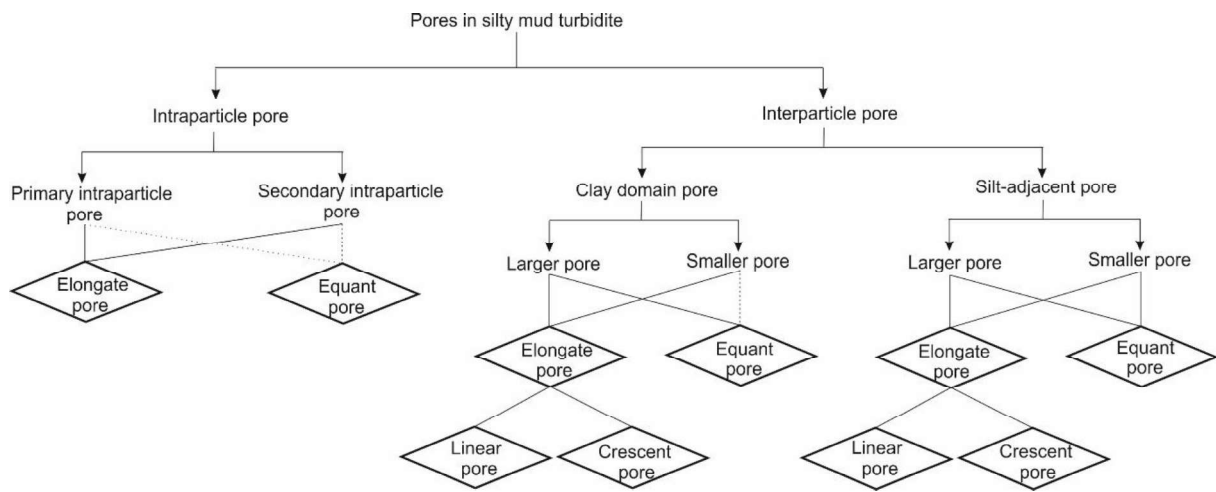
987



988 **Fig.3:** Porosity data for Units I (green dots), II (orange dots), and IIIA (blue dots). (a) BIB-SEM porosity - depth
 989 plot, (b) BIB-SEM porosity vs MAD porosity. Note: linear relationship that intersects origin. The data estimated
 990 by Hemes et al., 2013; Houben et al., 2014; Oelker et al., 2019 also follow similar trend. However, the data
 991 estimated by Nole et al., 2016 is deviated from the general trend.

992

993



994

995

996 **Fig.4:** Classification scheme adopted to demonstrate pore reduction mechanics with increasing compactional
997 strain. Dashed lines indicate rare pore types.

998

999

1000

1001

1002

1003

1004

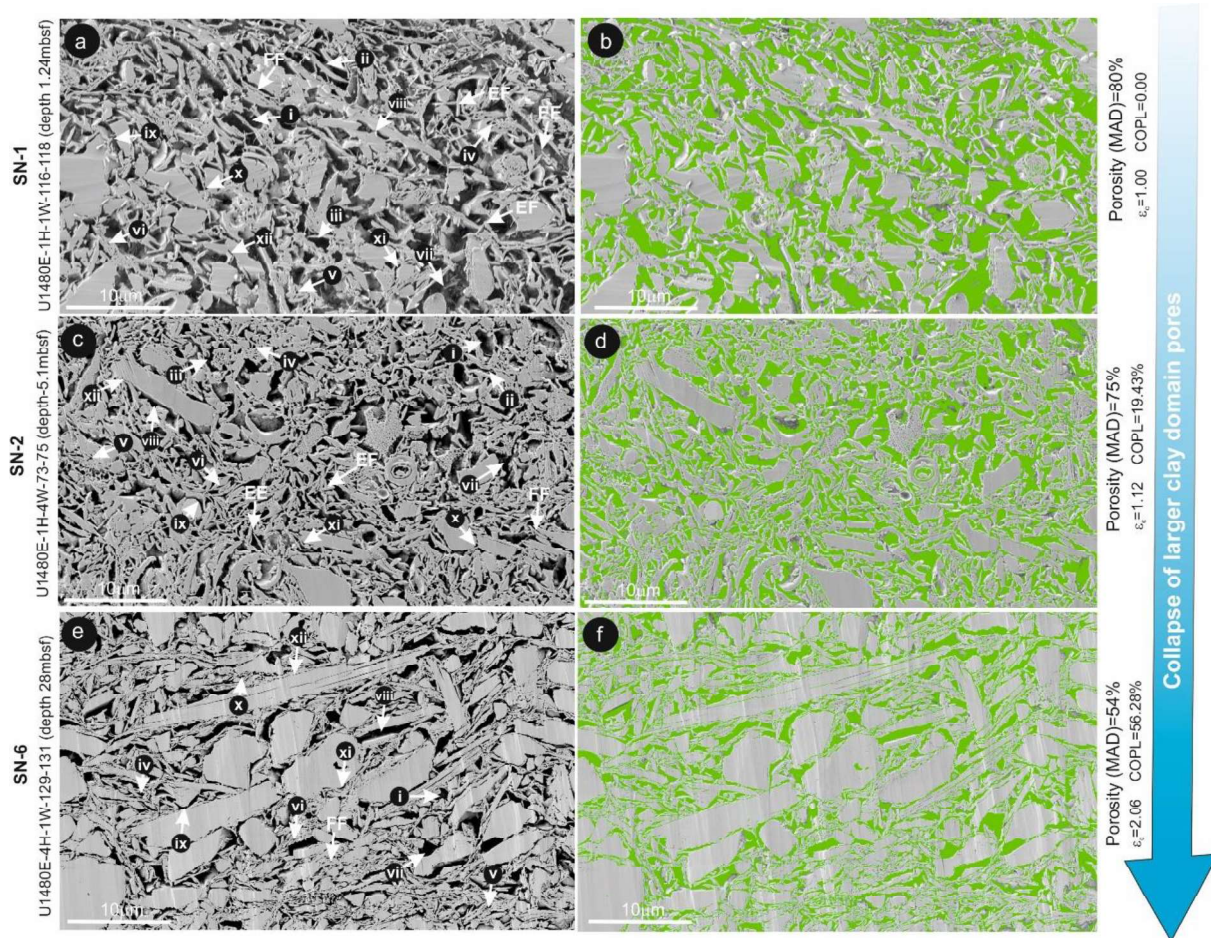
1005

1006

1007

1008

1009



1010

1011 **Fig.5:** Microstructural overview (BIB-SEM) of samples SN-1 (a and b), SN-2 (c and d), and SN-6 (e and f). Green
 1012 color represents segmented pores of the corresponding microstructure of sample. i = Equant large clay domain
 1013 pores, ii = elongated large clay domain pores, iii = Crescent-shaped large clay domain pores, iv = equant small
 1014 clay domain pores, v = Crescent-shaped small clay domain pores, vi = elongated small clay domain pores, vii =
 1015 Equant large silt-adjacent pores, viii = elongated large silt-adjacent pores, ix = Crescent-shaped large silt-adjacent
 1016 pores, x = equant small silt-adjacent pores, xi = Crescent-shaped small silt-adjacent pores, xii = elongated small
 1017 silt-adjacent pores. **EE= Edge to edge contact, EF=Edge to face contact, and FF=Face to face contact.**

1018

1019

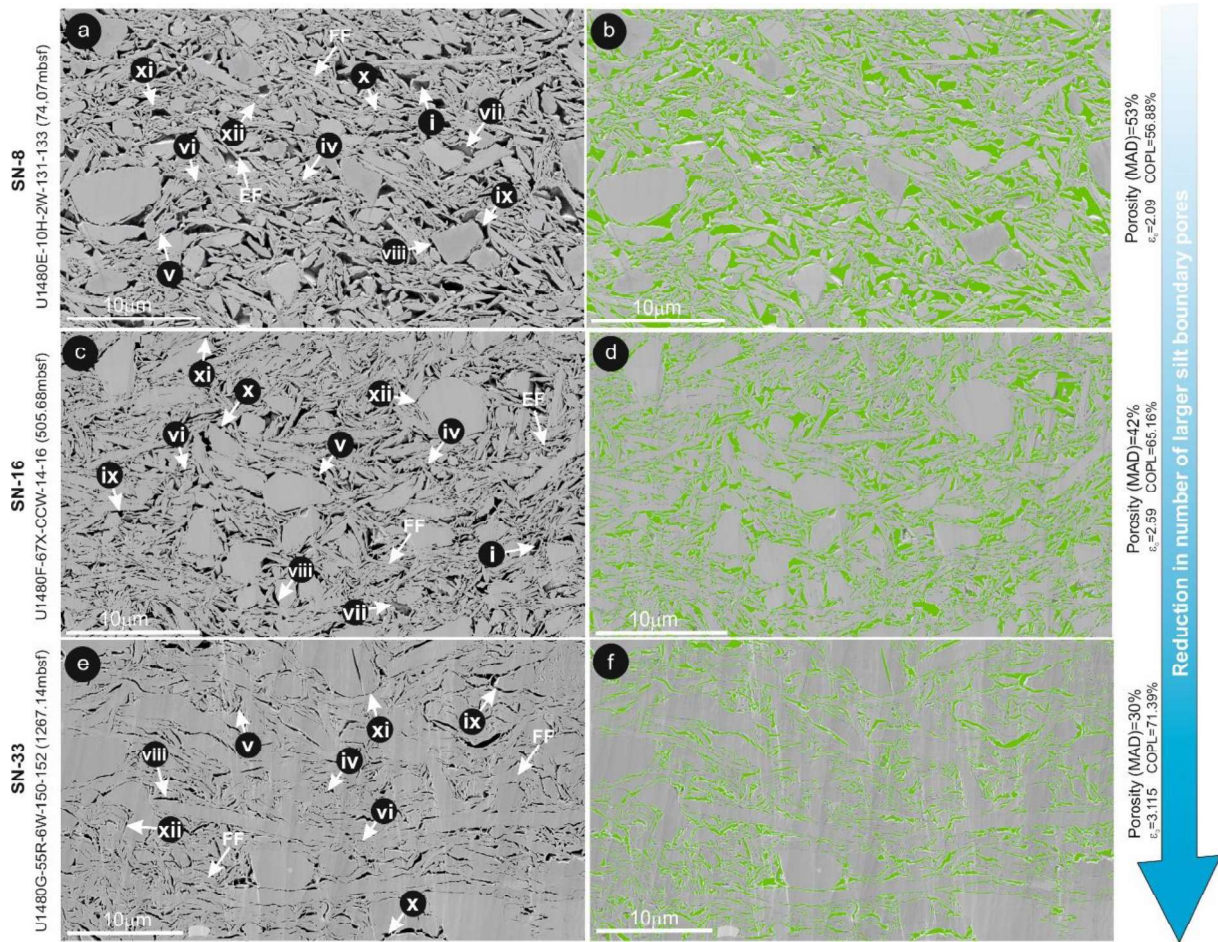
1020

1021

1022

1023

1024



1025

1026 **Fig.6:** Microstructural overview (BIB-SEM) of samples SN-8 (a and b), SN-16 (c and d), and SN-32 (e and f).
 1027 Green color represents segmented pores of the corresponding microstructure of sample. i = Equant large clay
 1028 domain pores, ii = elongated large clay domain pores, iii = Crescent-shaped large clay domain pores, iv = equant
 1029 small clay domain pores, v = Crescent-shaped small clay domain pores, vi = elongated small clay domain pores,
 1030 vii = Equant large silt-adjacent pores, viii = elongated large silt-adjacent pores, ix = Crescent-shaped large silt-
 1031 adjacent pores, x = equant small silt-adjacent pores, xi = Crescent-shaped small silt-adjacent pores, xii = elongated
 1032 small silt-adjacent pores. **FF= Face to face contact, EF= Edge to face contact.**

1033

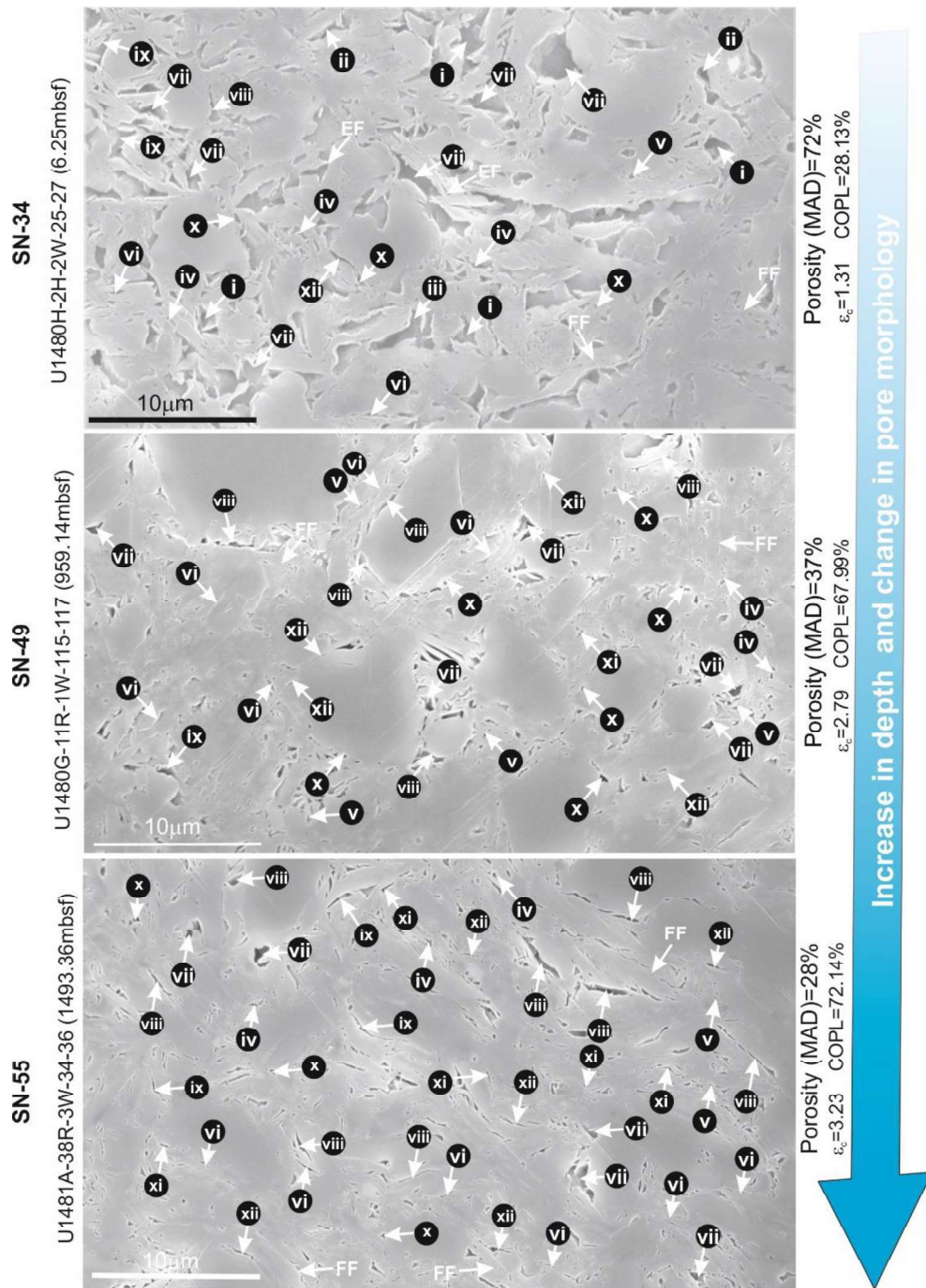
1034

1035

1036

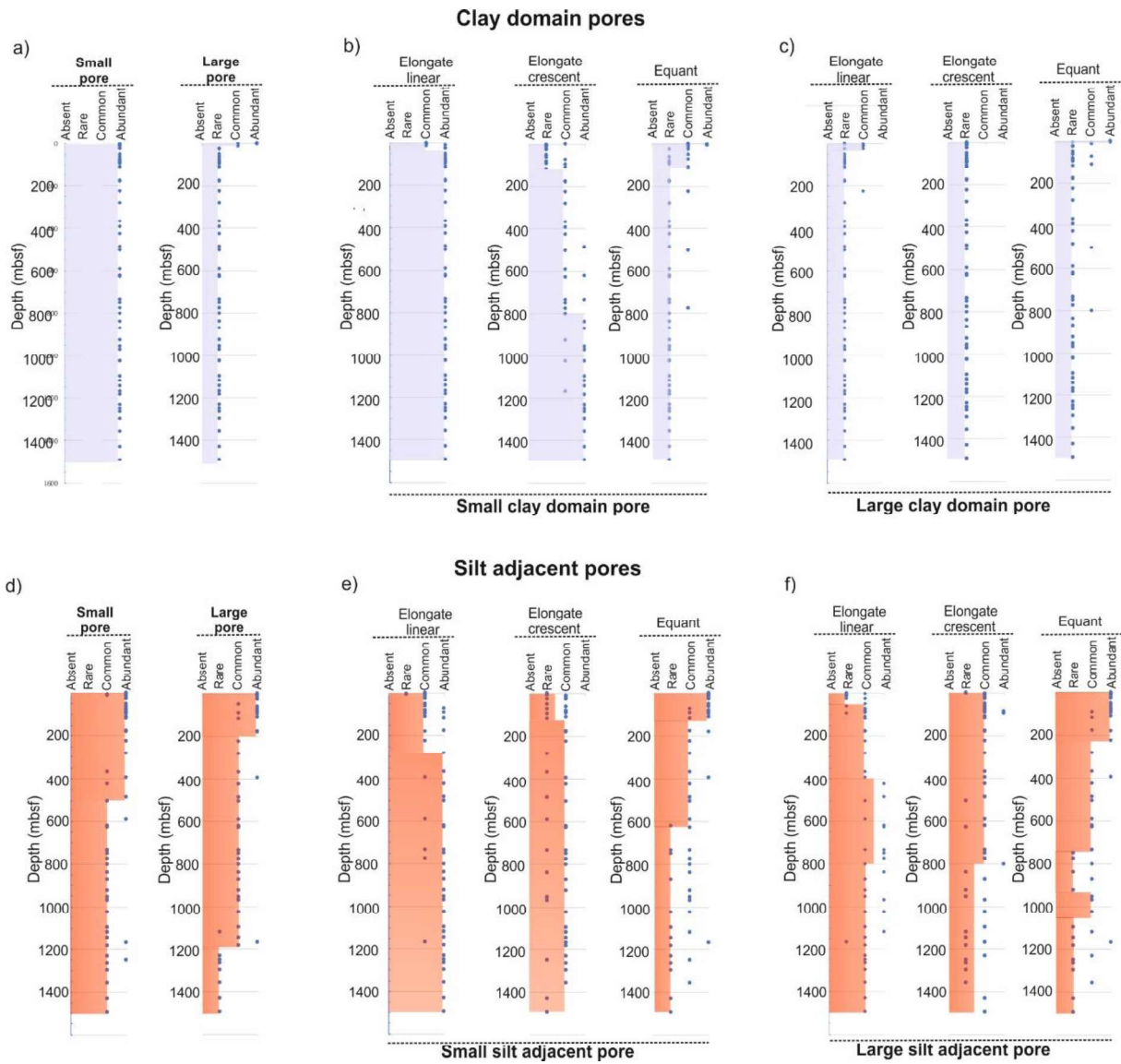
1037

1038



1040

1041 **Fig.7:** Microstructural overview (Field Emission SEM) of samples SN-34, SN-49, and SN-55. i = Equant large
 1042 clay domain pores, ii = elongated large clay domain pores, iii = Crescent-shaped large clay domain pores, iv =
 1043 equant small clay domain pores, v = Crescent-shaped small clay domain pores, vi = elongated small clay domain
 1044 pores, vii = Equant large silt-adjacent pores, viii = elongated large silt-adjacent pores, ix = Crescent-shaped large
 1045 silt-adjacent pores, x = equant small silt-adjacent pores, xi = Crescent-shaped small silt-adjacent pores, xii =
 1046 elongated small silt-adjacent pores. **FF= Face to face contact, EF= Edge to face contact.**



1048

1049 **Fig.8:** Pore type summary for clay domain (a-c) and silt-adjacent (d-f) pore types. (a) abundance of small and large
 1050 clay domain pores; (b) and (c) depth progression of small and large clay domain pore morphologies; (d) abundance
 1051 of small and large silt-adjacent pores; (e) and (f) depth progression of small and large clay domain pore
 1052 morphologies. Abundant = >25% pores, common = 2%-25% pores, rare = 0-2% pores, absent = not observed.

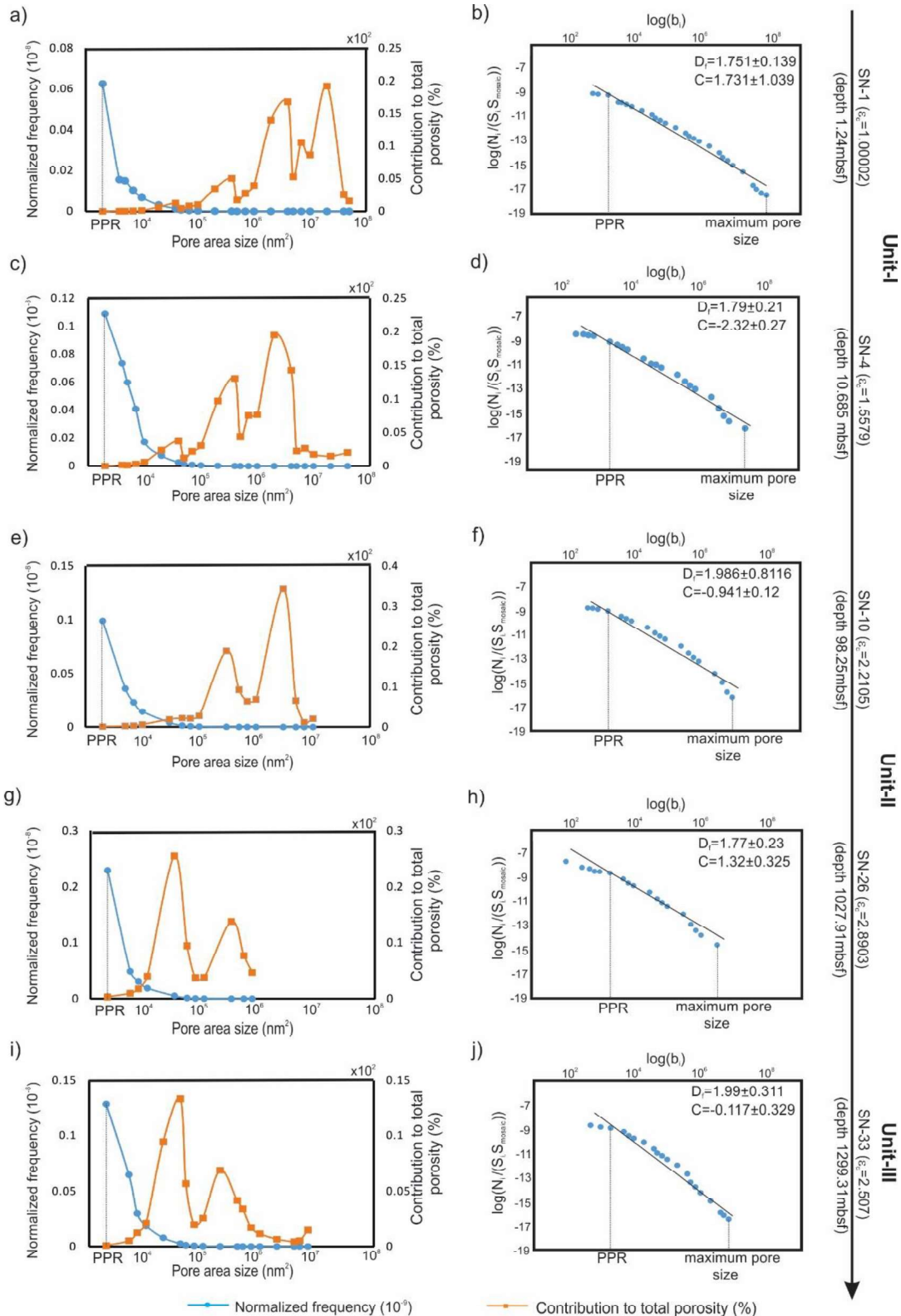
1053

1054

1055

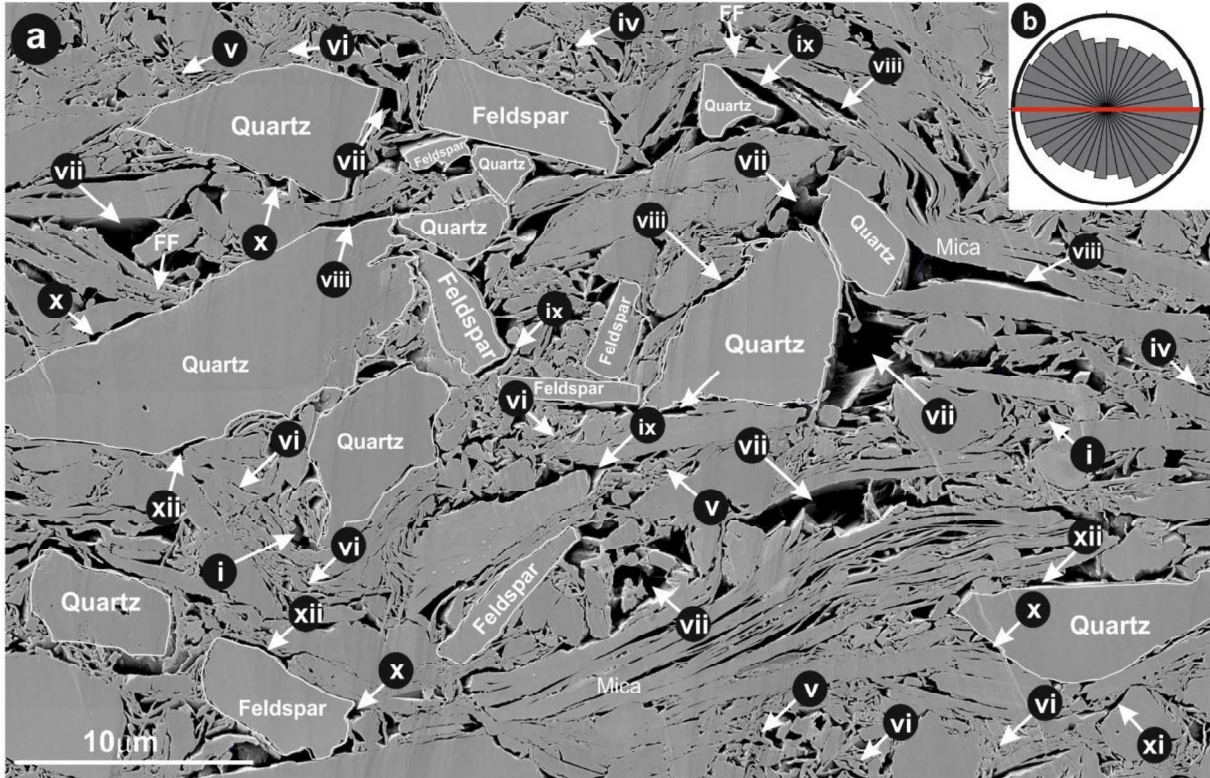
1056

1057



1059 **Fig.9:** Pore size distribution defined by pore area. Left column: normalized frequency (blue) and contribution to
 1060 total porosity (orange). Right column: pore size-frequency log-log distribution. Power-law between PPR and
 1061 maximum pore size interpreted as black line with corresponding regression parameters. Sample number, depth,
 1062 and compaction strain defined along right side of diagram

SN- 29 (U1480G-45R-1W-93-95, depth 1172.88mbsf)



1064

1065

1066 **Fig.10:** Silt-rich sample (SN-29; 1173 mbsf) (a) i = Equant large clay domain pores, ii =elongated large clay
1067 domain pores, iii = Crescent-shaped large clay domain pores, iv = equant small clay domain pores, v = Crescent-
1068 shaped small clay domain pores, vi = elongated small clay domain pores, vii = Equant large silt-adjacent pores,
1069 viii = elongated large silt-adjacent pores, ix = Crescent-shaped large silt-adjacent pores, x =equant small silt-
1070 adjacent pores, xi = Crescent-shaped small silt-adjacent pores, xii = elongated small silt-adjacent pores.(b) Rose
1071 diagram of long axes of pores (bedding = red line). **FF= face to face contact of clay particles.**

1072

1073

1074

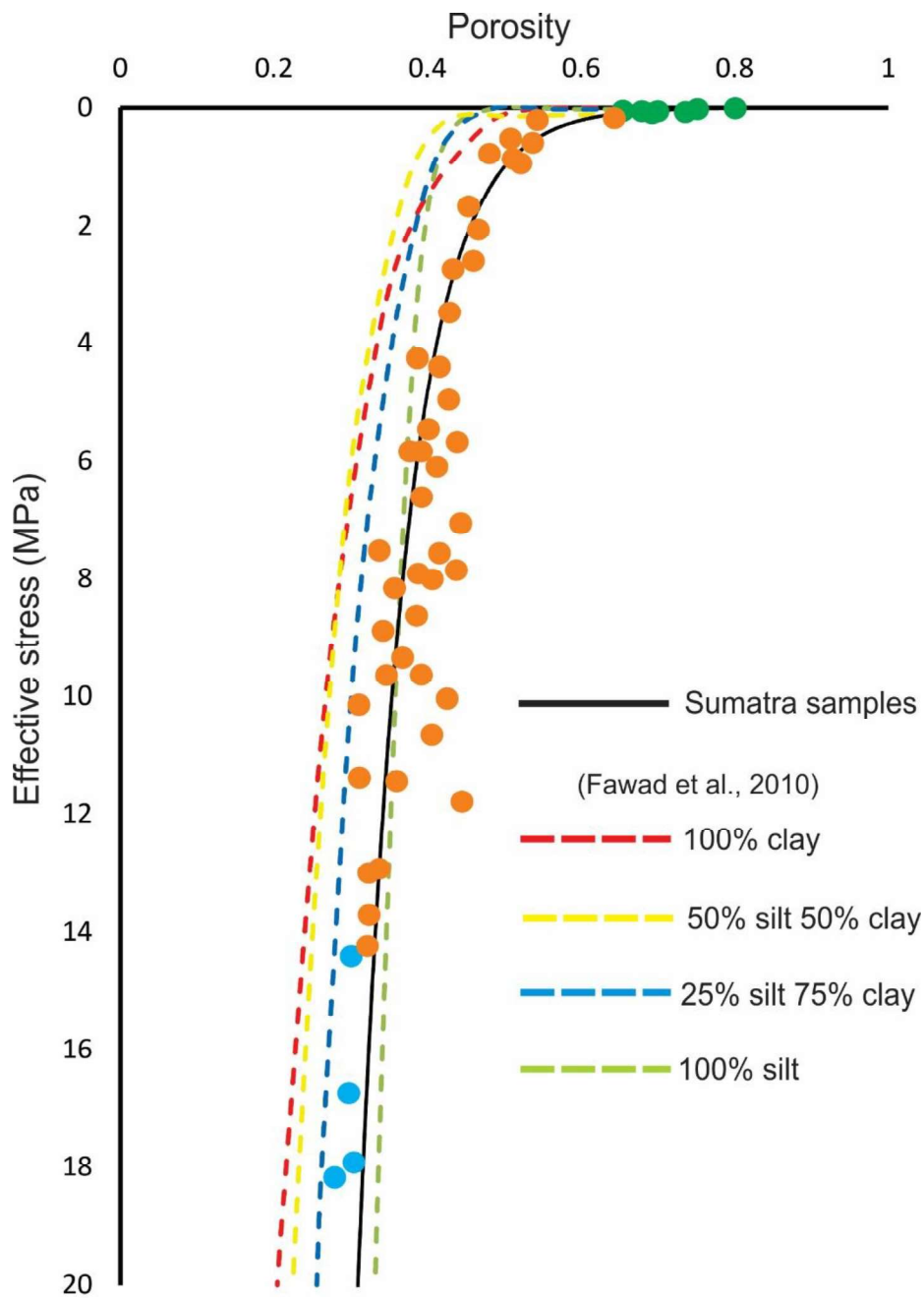
1075

1076

1077

1078

1079



1081

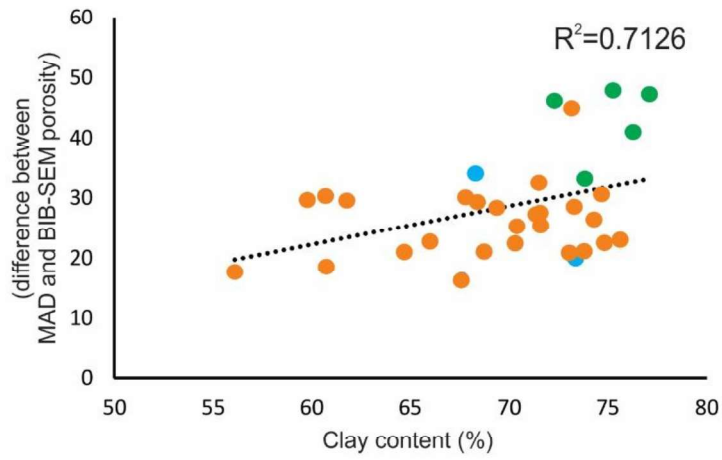
1082 **Fig.11:** Effective stress vs porosity (MAD) for experimental mixtures of clay and silt (dashed lines; Fawad et al.,
 1083 2010) compared with Sumatra data (Unit 1 = green; Unit II = orange; Unit III = blue). Solid black solid line is a
 1084 best-fit data regression for Sumatra samples.

1085

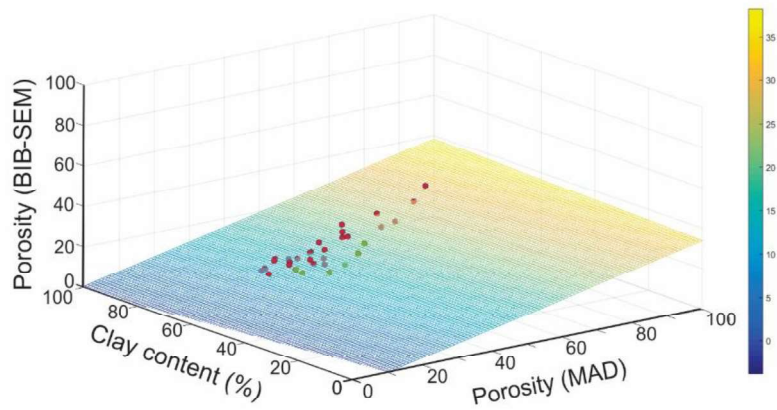
1086

1087

a)



b)



- samples exhibit higher clay content
- samples exhibit lower clay content and higher interaggregate pores

1089

1090 **Fig.12:** (a) Clay content vs difference between MAD and BIB-SEM porosity. (b) Multivariate regression
 1091 analysis using three parameters: BIB-SEM porosity, clay content, and MAD porosity (33 samples).

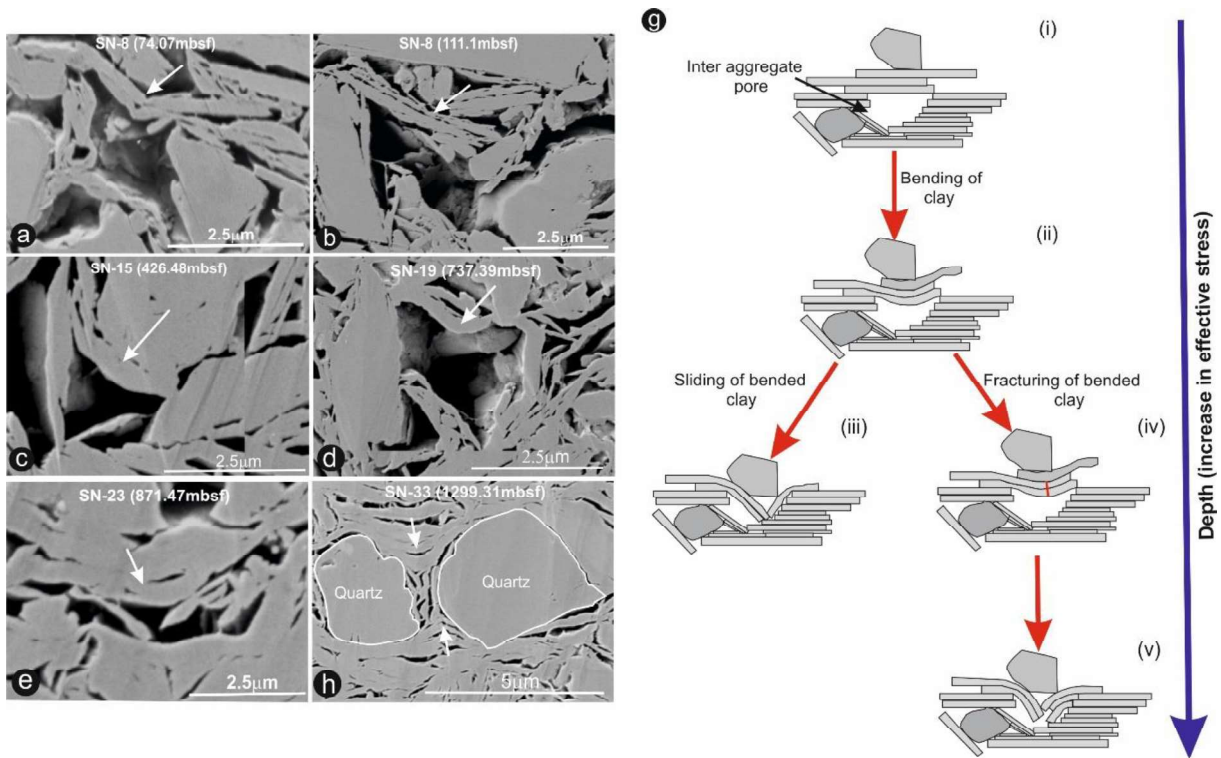
1092

1093

1094

1095

1096



1097

1098 **Fig.13:** a-f: examples of bent clay particles on top of silt-adjacent larger pores; sample ID and depth labelled on
1099 photos. (g) Micromechanical model for collapse of large silt-adjacent pores.

1100

1101

1102

1103

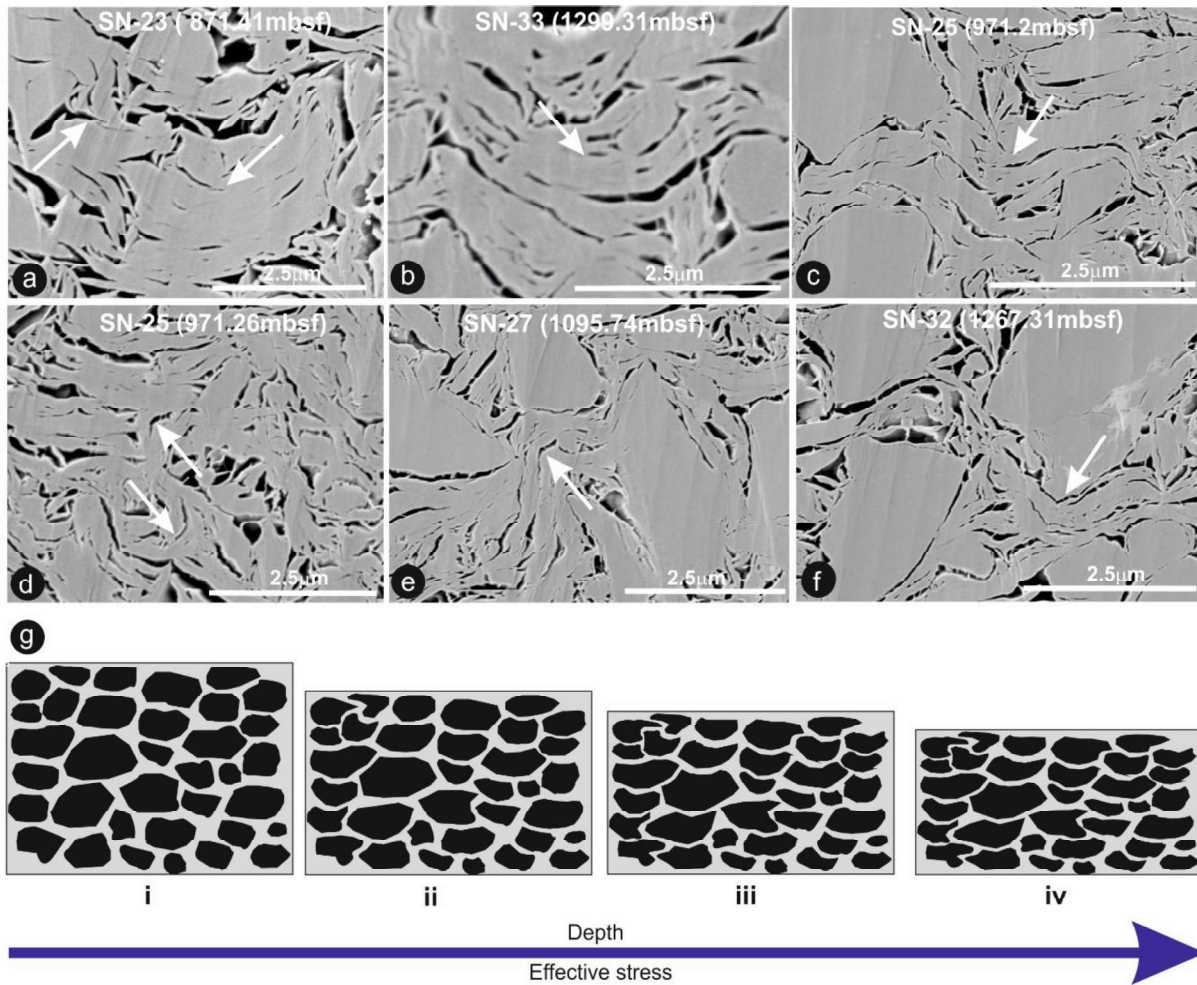
1104

1105

1106

1107

1108



1109

1110 **Fig.14:** a-f: examples of clay aggregate bending (white arrows). (g) Conceptual diagram tracing porosity reduction
 1111 and increase in preferred alignment of the long axes of pores by bending of clay perpendicular to applied vertical
 1112 stress.

1113

1114

1115

1116

1117

1118

1119

1120

1121

Table 1: Clay mineralogy in subunits of the Sumatra succession

Drilling site	Units	Smectite (%)	Illite (%)	I/S expandability (%)
U1480	Unit-I	33	49	62
	Unit-II	17	59	63.5
	Unit-IIIA	73	19	88
U1481	Unit-II	20.66	58.41	64
	Unit-III	36.36	46.78	73

1122

1123

1124

1125

1126

1127

1128

1129

1130

1131

1132

1133

1134

1135

Table 2: Porosity data estimated using BIB-SEM approach from Aachen sample sets. D=fractal dimension, C=statistical constant

Units	Sample no	Depth (mbsf)	Shipboard moisture and density data (MAD)				Secondary electron image analysis (SE2)										BSE image analysis		
			MAD porosity	Compact ion strain	COP	Magnification	Area imaged (µm ²)	Pixel size (nm)	REA (µm ²)	Number of pores detected	Porosity	Statistical analysis of pores			Magnification of BSE images	Clay +muscovite	Mineral percentage (%)		
Unit-I	SN-1	1.24	80	1.00	0.00	20000x	7586.36	14.22	65 x 65	6046	32	1.750+-0.139	1.731+-1.039	10000x	77.08	22.92			
	SN-2	5.1	75	1.12	19.43	20000x	11028.86	14.22	60 x 60	23985	27	1.89+-0.473	-1.37+-0.112	10000x	75.26	24.74			
	SN-3	9.18	67	1.46	38.19	20000x	10926.87	14.22	70 x 70	31488	21	1.84+-0.5066	-1.72+-0.185	10000x	72.29	27.71			
	SN-4	10.685	65	1.56	42.12	20000x	11174.25	14.22	65 x 65	17124	24	1.79+-0.21	-2.32+-0.27	10000x	76.28	23.72			
	SN-5	26.05	64	1.61	44.08	20000x	9178.23	14.22	75 x 75	15410	19	1.89+-0.26	1.42+-0.138	10000x	73.14	26.86			
	SN-6	28	54	2.06	56.28	20000x	14283.99	14.22	80 x 80	25105	23	1.76+-0.17	2.47+-0.02	10000x	74.68	25.32			
	SN-7	63.24	50	2.22	59.38	10000x	9532.30	14.22	70 x 70	17624	21	1.822+-0.2	2.11+-0.553	10000x	61.77	38.23			
Unit-IIA	SN-8	74.07	53	2.09	56.88	20000x	6295.64	14.22	75 x 75	14480	20	1.964+-0.466	1.861+-0.120	10000x	73.83	26.17			
	SN-9	87.98	48	2.34	61.46	20000x	12092.80	14.22	70 x 70	19435	17	1.873+-0.306	1.692+-0.157	10000x	60.69	39.31			
	SN-10	98.25	51	2.21	59.21	20000x	8945.04	14.22	70 x 70	17003	21	1.986+-0.8116	-0.941+-0.12	10000x	68.37	31.63			
	SN-11	111.1	51	2.17	58.47	20000x	11796.13	14.22	75 x 75	35322	19	1.8353+-0.22	1.21+-0.56	10000x	71.5	28.5			
Unit-IB	SN-12	176.5	45	2.47	63.52	20000x	11162.07	14.22	70 x 70	18619	16	1.93+-0.20	0.918+-0.43	10000x	69.37	30.63			
	SN-13	226.7	46	2.41	62.57	20000x	10095.85	14.22	80 x 80	29038	18	1.87+-0.1383	-1.471+-0.36	10000x	73.28	26.72			
	SN-14	369.19	42	2.57	64.98	20000x	11096.09	14.22	65 x 65	26650	15	1.876+-0.140	-1.09+-0.271	10000x	71.47	28.53			
	SN-15	426.68	38	2.77	67.50	20000x	11424.39	14.22	60 x 60	31589	15	1.79+-0.26	1.41+-0.32	10000x	66	34			
	SN-16	505.32	42	2.59	65.16	20000x	11601.30	14.22	80 x 80	36607	15	1.76+-0.34	1.42+-0.72	10000x	71.4	28.6			
	SN-17	592.42	43	2.54	64.47	20000x	13552.14	14.22	85 x 85	16792	14	1.87+-0.19	1.14+-0.13	10000x	59.79	40.21			
	SN-18	630.55	39	2.75	67.20	20000x	14205.79	14.22	70 x 70	29208	13	1.866+-0.175	-0.513+-0.19	10000x	65.39	34.61			
Unit-IB	SN-19	737.39	35	2.90	68.89	20000x	11929.89	14.22	65 x 65	30132	12	1.848+-0.26	-0.342+-0.41	10000x	75.61	24.39			
	SN-20	751.16	38	2.76	67.38	20000x	9912.07	14.22	70 x 70	26299	12	1.874+-0.09	-0.213+-0.21	10000x	74.28	25.72			
	SN-21	776.17	34	2.97	69.67	20000x	9892.76	14.22	45 x 45	22878	13	1.98+-0.13	0.427+-0.20	10000x	73.71	26.29			

Table 2: Continued

Units	Sample no	Depth (msf)	Shipboard moisture and density data (MAD)				Secondary electron image analysis (SE2)						BSE image analysis			
			MAD porosity	Compact ion strain	COPL	Magnification	Area imaged (µm ²)	Pixel size (nm)	REA (µm ²)	Number of pores detected	Porosity	D	C	Magnification of BSE images	Clay +muscovite	Mineral percentage (%)
	SN-22	802.55	43	2.54	64.4	20000x	10165.03	14.22	70 x 70	10083	13.72	1.897+ -0.17	-1.201+-0.27	10000x	67.77	32.23
	SN-23	871.87	34	2.95	69.4	20000x	11355.68	14.22	65 x 65	31864	13.45	1.86+ 0.22	1.469+-0.13	10000x	68.72	31.28
	SN-24	929.81	39	2.75	67.1	20000x	10278.30	14.22	50 x 50	32360	13.48	1.94+ 0.16	1.245+-1.36	10000x	71.58	28.42
	SN-25	971.26	31	3.11	71.0	20000x	10786.43	14.22	65 x 65	13428	10.51	1.83+ 0.107	0.512+-0.15	10000x	73.09	26.91
	SN-26	1027.9	35	2.89	68.8	20000x	12391.74	14.22	50 x 50	33593	13.59	1.77+ 0.23	1.32+-0.325	10000x	70.27	29.73
	SN-27	1095.7	32	3.06	70.5	20000x	7531.43	14.22	60 x 60	8502	9.78	1.725+ -0.32	1.45+-0.613	10000x	74.79	25.21
Unit-II	SN-28	1119.7	33	3.01	70.0	20000x	11980.58	14.22	60 x 60	30150	12.37	1.85+ 0.1746	1.37+-1.41	10000x	64.69	35.31
	SN-29	1172.8	36	3.05	68.6	10000x	46906.74	28.47	90 x 90	133051	12.65	1.83+ 0.18	-2.725+-0.23	10000x	56.1	43.9
	SN-30	1184.3	27	3.25	72.2	20000x	11815.07	14.22	50 x 50	24133	11.52	1.85+ 0.26	-0.451+-0.29	10000x	67.59	32.41
	SN-31	1233.1	32	3.06	70.5	20000x	11479.30	14.22	70 x 70	26793	13.64	1.73+ 0.18	1.241+-0.341	10000x	60.74	39.26
	SN-32	1267.1	30	3.15	71.3	20000x	11665.10	14.22	70 x 70	32933	9.96	1.87+ 0.1376	0.1165+ 1.210	10000x	73.29	26.71
Unit-III	SN-33	1299.3	44	2.51	64.0	20000x	7132.13	14.22	60 x 60	18350	10.47	1.99+ 0.311	-0.117+-0.329	10000x	68.31	31.69